



Permeability evolution during triaxial compaction of an anisotropic porous sandstone

Patrick Baud, Philip Meredith, Edward Townend

► To cite this version:

Patrick Baud, Philip Meredith, Edward Townend. Permeability evolution during triaxial compaction of an anisotropic porous sandstone. *Journal of Geophysical Research: Solid Earth*, 2012, 117, pp.B05203. hal-00746035

HAL Id: hal-00746035

<https://hal.science/hal-00746035>

Submitted on 16 Jun 2021

HAL is a multi-disciplinary open access archive for the deposit and dissemination of scientific research documents, whether they are published or not. The documents may come from teaching and research institutions in France or abroad, or from public or private research centers.

L'archive ouverte pluridisciplinaire **HAL**, est destinée au dépôt et à la diffusion de documents scientifiques de niveau recherche, publiés ou non, émanant des établissements d'enseignement et de recherche français ou étrangers, des laboratoires publics ou privés.

Copyright

Permeability evolution during triaxial compaction of an anisotropic porous sandstone

Patrick Baud,¹ Philip Meredith,² and Edward Townend^{2,3}

Received 19 January 2012; revised 25 March 2012; accepted 26 March 2012; published 10 May 2012.

[1] In this paper we report results from an experimental study into the influence of pre-existing structural anisotropy on deformation localization and permeability evolution during triaxial compaction of a porous sandstone. Diemelstadt sandstone was selected for this study because it exhibited significant structural anisotropy as measured by AMS and P and S-wave velocities. This resulted in significant mechanical anisotropy, with samples deformed parallel to bedding being always stronger in the compactant regime than samples deformed normal to bedding. Permeability decreases were also larger (by about an order of magnitude) and far more abrupt in samples deformed normal to bedding. Microstructural analysis of deformed samples revealed that both the mechanical anisotropy and the differences in permeability evolution can be explained by the different geometrical attributes of the compaction bands that propagated in the two orientations. Bedding-parallel compaction bands developed at lower stresses and were more tabular and less tortuous than bands that developed at oblique angles to bedding. Bands appear to have a similar thickness regardless of orientation, and we estimated a permeability contrast of about 3 orders of magnitude between the host rock matrix and the compaction bands. Our new data suggest that pre-existing structural anisotropy in a sandstone formation may play a major role in the development of compaction localization and its influence on fluid flow. Our laboratory results generally compare well with attributes of compaction bands observed in the field.

Citation: Baud, P., P. Meredith, and E. Townend (2012), Permeability evolution during triaxial compaction of an anisotropic porous sandstone, *J. Geophys. Res.*, 117, B05203, doi:10.1029/2012JB009176.

1. Introduction

[2] The evolution of permeability associated with the mechanical compaction of porous sandstone is of fundamental importance for many applications linked to reservoir/aquifer production, fault and earthquake mechanics and the geological storage of hazardous waste. For example, key issues in petroleum geoscience, such as prediction of reservoir deformation and fluid flow, hinge on realistic estimation of permeability and its evolution as a function of changing stress, strain and porosity. These issues are exacerbated by the significant level of hydro-mechanical coupling that can occur during both reservoir depletion [Boutéca *et al.*, 2000] and water injection [Heffer, 2002]. As a result, the U.S.

Department of Energy identified rock transport properties, fluid isolation and trapping, and fluid-enhanced rock deformation as priority research themes in its report on Basic Research Needs for Geosciences: Facilitating 21st Century Energy Systems [Department of Energy, 2007].

[3] Much insight into the coupling between deformation and pore fluids has been gained from laboratory studies; in particular in establishing relationships between deformation and permeability [David *et al.*, 1994; Zhu *et al.*, 1997; Keaney *et al.*, 1998; Wong and Zhu, 1999; Heiland and Raab, 2001; Main *et al.*, 2001; Mitchell and Faulkner, 2008; Dautriat *et al.*, 2009]. For porous sandstone, the systematic study of Zhu and Wong [1997] revealed the complex evolution of porosity and permeability during triaxial compression. They showed that while porosity and permeability both decrease in a positively correlated way during compactant cataclastic flow, the same parameters are negatively correlated in the brittle faulting regime, as permeability was found to decrease during dilatancy and strain localization while porosity increased.

[4] In the compactant regime, permeability reduction can be influenced significantly by whether the nature of the inelastic deformation is homogeneous (distributed) or heterogeneous (localized). For this reason, the development of localized compaction bands (CBs) in porous sandstones has generated a great deal of interest within the geoscience

¹School and Observatory for Earth Sciences, Institut de Physique du Globe de Strasbourg, UMR 7516, CNRS, Université de Strasbourg, Strasbourg, France.

²Rock and Ice Physics Laboratory, Department of Earth Sciences, University College London, London, UK.

³Now at Shell Oil Company, Houston, Texas, USA.

Corresponding author: P. Baud, School and Observatory for Earth Sciences, Institut de Physique du Globe de Strasbourg, UMR 7516, CNRS, Université de Strasbourg, 5 rue Rene Descartes, F-67084 Strasbourg, France. (patrick.baud@unistra.fr)

Copyright 2012 by the American Geophysical Union.
0148-0227/12/2012JB009176

community. Field observations of CBs in sandstone formations [Hill, 1989; Mollema and Antonellini, 1996; Sternlof et al., 2005; Aydin and Ahmadov, 2009; Schultz, 2009; Eichhubl et al., 2010] showed significant local porosity reduction in these tabular structures that are generally oriented normal or sub-normal to the maximum principal stress. Indeed, fluid flow simulations based on the petrophysical characteristics, geometric attributes and distribution of CBs have revealed potential impacts at the reservoir/aquifer scale [Eichhubl et al., 2004; Borja and Aydin, 2004; Sternlof et al., 2006].

[5] A number of laboratory studies of CB development have been undertaken over the past decade or so [Olsson and Holcomb, 2000; Klein et al., 2001; Baud et al., 2004; Fortin et al., 2005; Townend et al., 2008; Tembe et al., 2008; Charalampidou et al., 2011]. They show that CB development in the laboratory typically commences at the brittle-ductile transition and is associated with shear-enhanced compaction [Wong et al., 2001] and commonly also with enhanced output of acoustic emissions [Baud et al., 2004]. However, despite much progress being made over this period, a number of important questions still remain; specifically, in what way do microstructural characteristics control the evolution and geometry (orientation, tortuosity) of CBs and, in turn, how does the presence of CBs influence permeability and fluid flow in reservoirs [Holcomb et al., 2007]?

[6] Tembe et al. [2008] noted that even slight variations in bedding orientation influenced the overall orientation of CBs in a number of their Diemelstadt sandstone samples. Furthermore, a pilot study by Louis et al. [2009] showed that in a rock with strong bedding inhomogeneity, compaction localization was enhanced in some orientations and inhibited in others. Another study by Louis et al. [2007] combined X-ray computed tomography (CT) with quantitative microstructural measurements to show that CBs appeared to develop more readily in rocks with a relatively homogeneous microstructure. Results from network modeling [Katsman et al., 2005] and discrete element modeling [Wang et al., 2008] supported this view, and concluded that compaction localization is promoted by a relatively homogeneous microstructure. To date, the influence of CBs on permeability evolution has only been measured in a few rocks; Bentheim sandstone [Vajdova et al., 2004] and Bleurwiller sandstone [Fortin et al., 2006]. However, both studies report a permeability contrast of up to two orders of magnitude between the host rock and the compaction bands.

[7] To our knowledge, there remains a paucity of laboratory data describing how the juxtaposition of anisotropic principal stresses and the structural anisotropy caused by sedimentary bedding orientation influences the development of discrete CBs in sandstone. There also appears to be no data on how different orientations and geometric attributes of CBs influence fluid flow. In this paper, we try to address these gaps in knowledge by reporting a systematic study of the development of CBs in samples cored parallel and orthogonal to the bedding plane in a sandstone showing significant pre-existing structural anisotropy (Diemelstadt sandstone). We show that CBs develop in both orientations but that their geometric attributes are very different. In turn, these geometrical differences influence fluid flow in significantly different ways in the two orientations. Finally, we

compare our new data to previously published permeability data on deformed sandstone and with recently reported measurements on CBs in the field.

2. Sample Material and Its Characterization

[8] Diemelstadt sandstone (*Wrexener Buntsandstein*) was chosen for this study because of its use in several previous studies [Fortin et al., 2005; Tembe et al., 2008]. Several blocks were collected from a quarry located near the town of Wrexen (Germany). For this study, we specifically selected the block that exhibited the highest degree of pre-existing structural anisotropy. As we show below, there are significant differences between our material and the material from the same quarry studied by Fortin et al. [2005] and Tembe et al. [2008] in terms of both petrographic and mechanical properties; and these rocks should, therefore, be considered as essentially different materials. However, all samples used in this study were cored from the same block of Diemelstadt sandstone as the samples used in the study of Townend et al. [2008].

[9] Our sample material had an average porosity of 23%, and an average grain size of 150 μm (Figure 1a). Its nominal composition is: 70% quartz, 10% lithics, 10% Feldspar, 5% Chlorite and 5% Muscovite. Grains are sub-rounded and moderately sorted, with primarily point contacts and occasional sutured contacts. Grains also show overgrowths of quartz cement with ghost edges of the original crystal faces remaining visible. Hematite staining around grain edges is inferred to be of post-diagenetic origin since no staining is observed at grain contacts. The textural maturity of Diemelstadt sandstone suggests a fluvial origin. X-ray computed tomography images of the intact material, acquired at a resolution of 40 μm (Figure 1b), reveal that the material is relatively homogeneous in spite of its sedimentary layering.

[10] For simplicity of discussion, we refer to the three principal orientations of our sample block as X, Y and Z; with Z being the direction normal to bedding and X and Y being orthogonal directions within the bedding plane. We used two different methods to quantify the anisotropy of the intact material: measurements of the anisotropy of magnetic susceptibility (AMS), and measurements of elastic wave velocity anisotropy.

[11] AMS measurements were made both on dry samples to determine the anisotropy of the solid matrix (mAMS) and on samples saturated with a magnetically susceptible ferrofluid to determine the total anisotropy of the matrix plus pore space (tAMS), following the method described in detail in Benson et al. [2003, 2005]. Measurements were made in 15 orientations on each of 22 samples using a KLY-2 susceptibility bridge (AGICO Instruments), and the anisotropy of the pore space (pAMS) was determined by subtracting mAMS values from tAMS values for each measurement. Principal susceptibility axes were then calculated by inverting the individual pAMS measurements and fitting them to an ellipsoid. The orientations of the principal pore space susceptibility axes are plotted on a lower-hemisphere stereographic projection in Figure 2a. The data show that the minimum axes occur in a tight cluster closely aligned with the Z direction, and that the intermediate and maximum axes are distributed in a narrow band around the XY plane and orthogonal to the minimum axes. The measurements

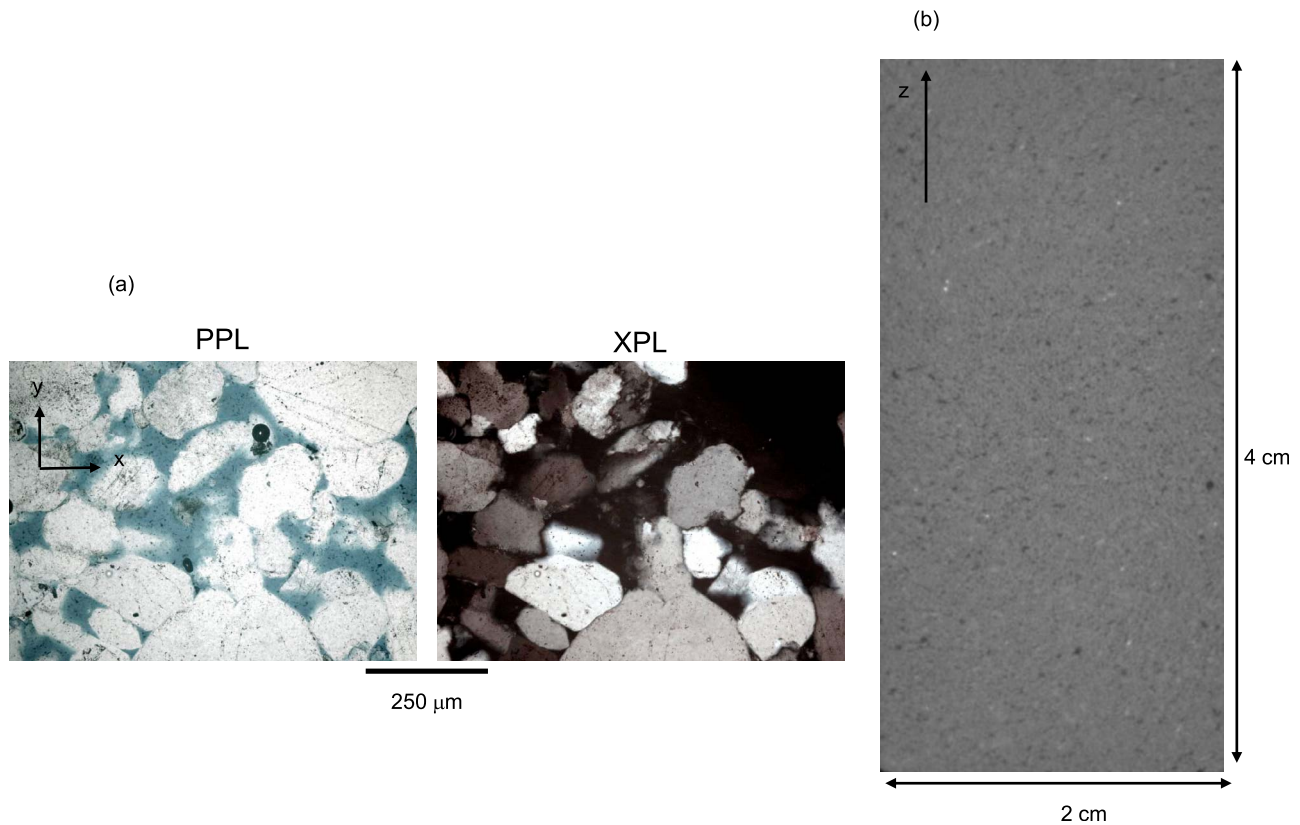


Figure 1. (a) Transmitted-light micrographs of Diemelstadt sandstone in the XY plane under plane polarized light (PPL) and cross-polarized light (XPL). (b) CT image of Diemelstadt sandstone acquired at a resolution of 40 μm .

show no obvious distinction between the intermediate and maximum axis orientations. The minimum, intermediate and maximum axes are all offset by between 6° and 12° from the Z direction (normal to bedding) and the XY plane (bedding plane), respectively. These offsets approximately equate to the dip of the visible cross-bedding in our Diemelstadt

sandstone samples. This suggests that the pore-fabric geometry is controlled by the cross-bedding fabric.

[12] In addition to providing the orientations of the three principal anisotropy axes, the pAMS technique can also provide the relative magnitudes of these axes. One useful way of representing the pore fabric anisotropy quantitatively

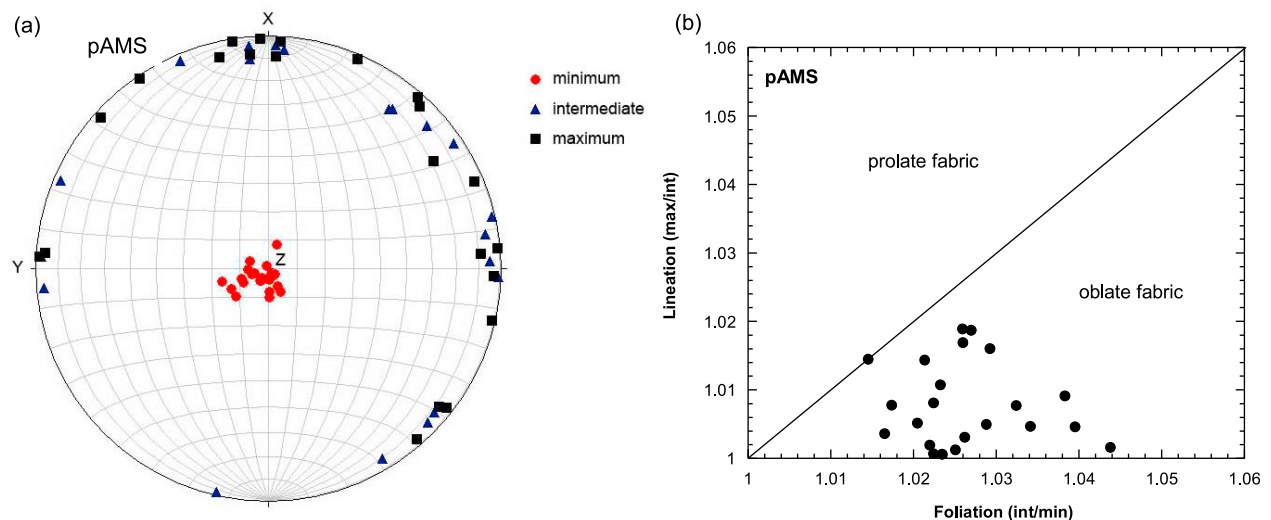


Figure 2. (a) Stereographic projection of pAMS data. Minimum principal axes are represented as red circles, intermediate axes as blue triangles, and maximum axes as black squares. (b) Flinn diagram for pAMS ellipsoids. The conditions corresponding to prolate and oblate fabric are indicated on the diagram.

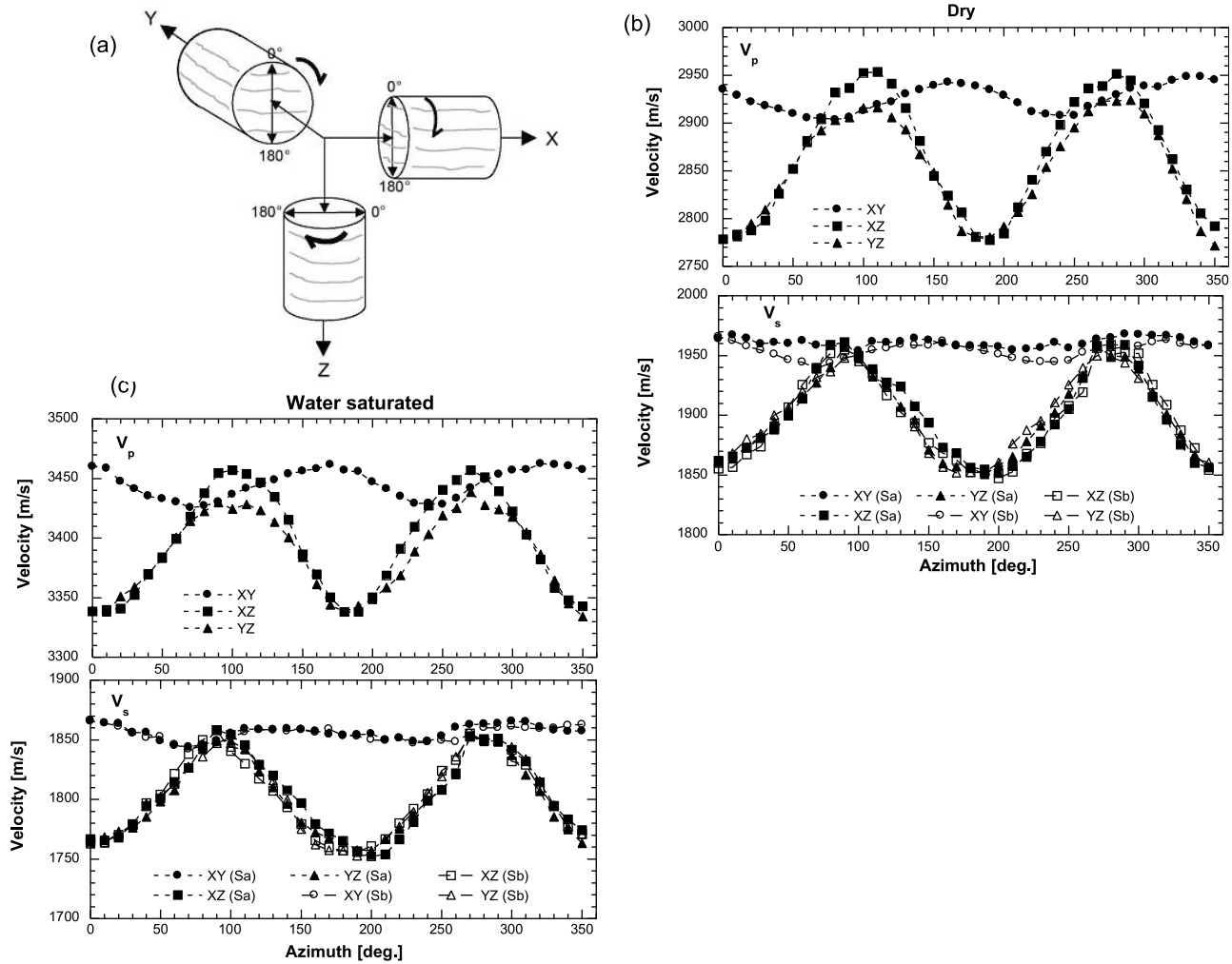


Figure 3. (a) A schematic core-set showing the reference axes and orientations used to make radial velocity measurements. Elastic wave velocity variations with azimuth for Diemelstadt sandstone under (b) dry conditions and (c) water-saturated conditions. For Sa waves (close symbols) the polarization direction is parallel to the core axis, and for Sb waves (open symbols), the polarization direction is orthogonal to the core axis. (d) Stereonets showing the principal directions for P and S-wave under dry (open symbols) and water-saturated (closed symbols) conditions. (e) Flinn plot of P wave and S-wave ellipsoid data. Open symbols represent dry conditions and closed symbols represent water-saturated conditions.

is by a Flinn diagram [Flinn, 1962] which plots the length ratio of the maximum to intermediate axes (representing lineation) against the length ratio of the intermediate to minimum axes (representing foliation). Applying Flinn's method to our data reveals a pore fabric that can be described as an oblate spheroid, as shown in Figure 2b. This is what is typically expected in a sedimentary rock as a result of the hydrodynamics of deposition followed by diagenetic compaction [Benson *et al.*, 2003].

[13] P and S-wave velocities were measured as a function of azimuth every 10° around three orthogonal cores under dry and water-saturated conditions (Figure 3a). Velocity data are presented in Figures 3b and 3c for dry and water-saturated samples, respectively. For all measurements, a clear and consistent variation with azimuth can be seen. The anisotropy is greatest for P wave velocities on dry samples (Figure 3b), with anisotropy being higher in the XZ and YZ planes that are normal to bedding (approximately 7%) and

lower in the XY plane that is parallel to bedding (less than 2%). The same general trends are observed for S-wave velocities, although the anisotropy is somewhat less pronounced. We also observe a similar general pattern for measurements made under water saturated conditions (Figure 3c). However, the average P wave velocity of saturated samples is about 18% higher than for dry samples, and the maximum P wave velocity anisotropy is lower at around 4%. This is entirely as expected, and is a result of the much higher bulk modulus of water as compared to air.

[14] Elastic wave velocity anisotropy was further quantified using the method of Louis *et al.* [2003]. We fitted the azimuthal velocities to an ellipsoid in order to allow the principal directions of P and S-wave velocity anisotropy to be visualized on a stereographic projection (Figure 3d) for direct comparison with the AMS data. As noted by Louis *et al.* [2003], this is strictly only correct for a second rank symmetric tensor, whereas elastic anisotropy is a fourth

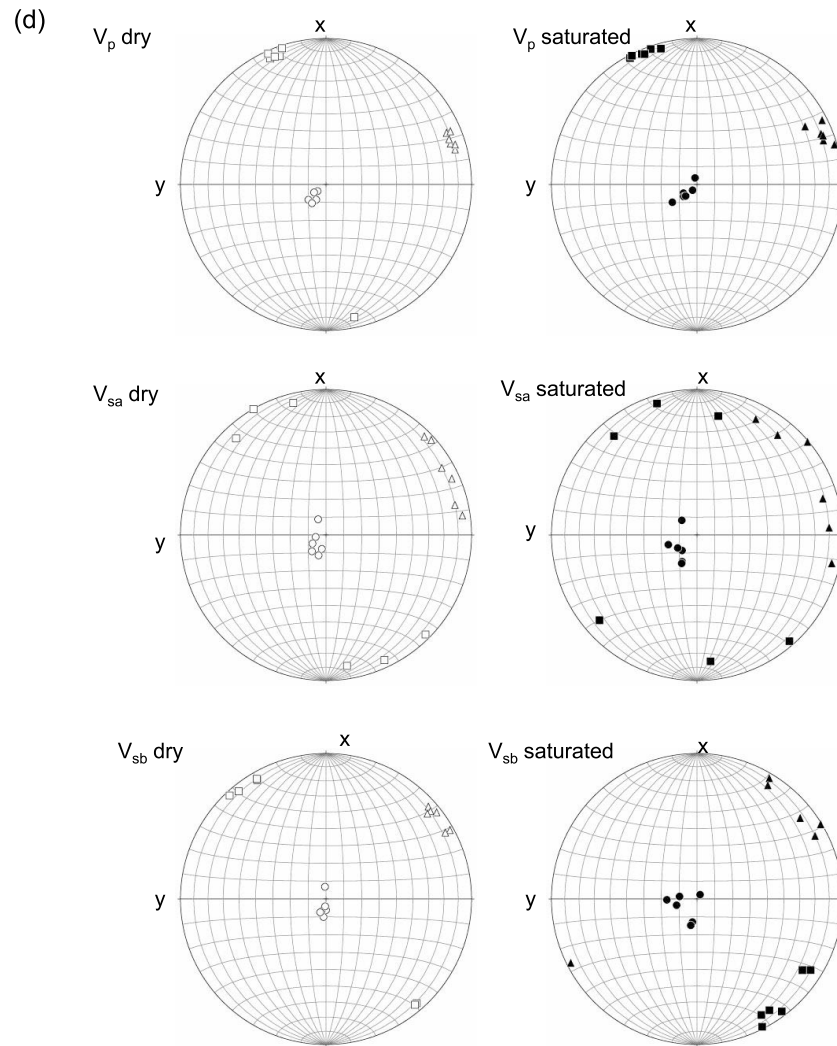


Figure 3. (continued)

rank tensor. However, as previously noted by *Benson et al.* [2003], the error in using the ellipsoidal approximation is less than the accuracy of the velocity measurements (approximately 1% for P waves and 2% for S-waves) and there is therefore no overall loss of accuracy. The principal velocity anisotropy axes show distributions which are in excellent general agreement with the principal axes derived from pAMS measurements (Figure 2a). The minimum axes are tightly grouped and fall sub-parallel to the Z axis with an average 10° offset (as for the pAMS data), with the intermediate and maximum axes occurring sub-parallel to the bedding (XY) plane. The magnitudes of the principal axes of the velocity ellipsoids are also used to construct a Flinn plot of lineation and foliation (Figure 3e) which again shows that the anisotropy can best be described as an oblate spheroid. The velocity measurements indicate an anisotropic fabric with a minimum principal axis oriented sub-normal to the bedding plane, in agreement with pAMS data. However, the intermediate and maximum principal axes of the pAMS data are scattered widely and interchangeably

sub-parallel to the bedding plane. By contrast, the velocity measurements exhibit clear clustering of the intermediate and maximum principal axes sub-parallel to the bedding plane but with a 90° offset between the clusters. This difference may arise from the fact that each technique is sensitive to different parameters. For example, elastic wave velocity measurements are sensitive to all elastic discontinuities, including narrow, low-aspect-ratio microcracks. By contrast, pAMS measurements are sensitive only to the bulk ferrofluid-filled porosity, and will therefore be less sensitive to low volume microcracks and more sensitive to high volume equant pores.

[15] Following the above measurements made under ambient laboratory conditions, we also made P and S-wave velocity and fluid permeability measurements at effective pressures up to 250 MPa on a set of three samples cored along the three principal orientations. The velocity measurements were made along the cylindrical axis of each sample using the same methodology as described in *Benson et al.* [2003], and the data are presented in Figure 4a.

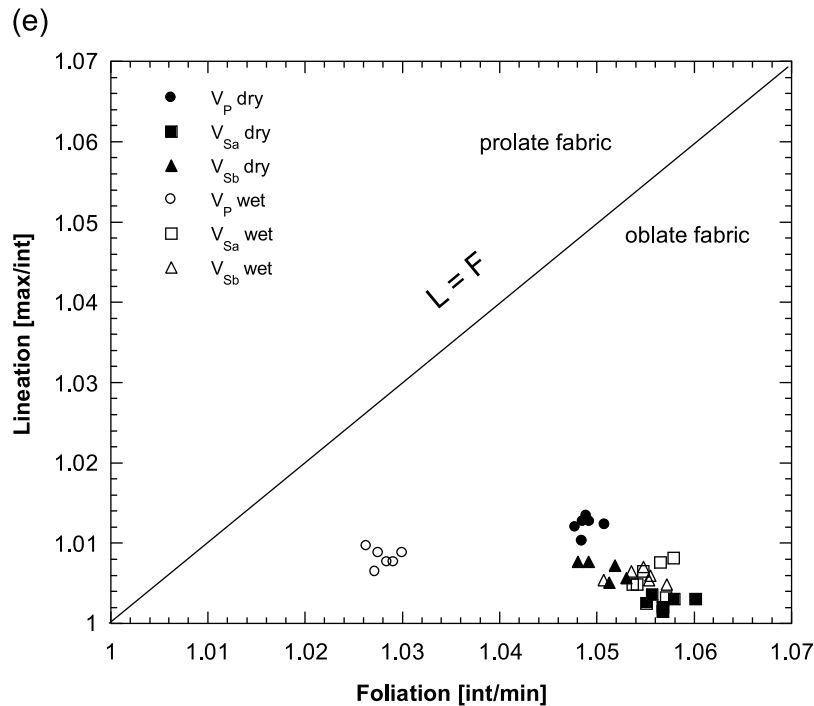


Figure 3. (continued)

Consistent with the ambient values, we see that the lowest velocities occur in the direction normal to bedding (Z axis), and that velocities parallel to bedding vary little with orientation. All velocities increase with increasing effective pressure, but the largest increases occur at the lower pressures. We also observe that the velocity anisotropy for both P-waves and S-waves decreases with increasing pressure (Figure 4b), but remained significant even at the highest pressures. Both observations are consistent with low aspect ratio microcracks closing at relatively low pressure, with the closure of higher aspect ratio microcracks and pores become progressively more difficult.

[16] We measured fluid permeability over the same effective pressure range using the steady state flow technique in a servo-controlled hydrostatic permeameter (see *Benson et al.* [2003, 2005] for details of the equipment and the technique). The data are presented in Figure 5, and show a modest but systematic permeability anisotropy, with permeability normal to bedding (along the Z axis) being $0.9 \times 10^{-12} \text{ m}^2$ and permeability parallel to bedding (along the X and Y axes) being higher at 1.3 to $1.4 \times 10^{-12} \text{ m}^2$. However, the permeability in each direction remains essentially constant over the whole pressure range. This suggests that the connectivity of the pore-space in Diemelstadt sandstone is not controlled by low aspect ratio microcracks, but by pore-throats that remain open even at the highest effective pressures applied.

[17] Overall, the acoustic and AMS measurements at ambient pressure show that our Diemelstadt sandstone can be characterized as exhibiting vertical transverse isotropy (VTI). Further, our acoustic and permeability measurements at elevated pressure show that the sandstone remains significantly anisotropic even at high pressure. This confirms that this is an appropriate material for the study of the impact

of anisotropy on CB development over a wide range of confining pressures.

3. Triaxial Deformation and Permeability Experiments

[18] All deformation and permeability experiments were performed at room temperature using the servo-controlled 400 MPa triaxial rock deformation apparatus in the Rock and Ice Physics Laboratory (RIPL) at University College London. All samples measured 40 mm in diameter by 100 mm long, and were cored parallel either to the Z direction or to the X direction. Accordingly, in the rest of this paper, samples deformed normal to bedding will be referred to as Z samples and samples deformed parallel to bedding will be referred to as X samples.

[19] Samples were mounted between two hardened steel end-caps in a nitrile rubber sleeve containing inserts for the mounting of acoustic emission transducers [*Heap et al.*, 2009]. During each experiment, axial strain was measured continuously using LVDT displacement transducers, and pore volume change was measured continuously using a servo-controlled pore fluid pressure intensifier and volumeter [*Benson et al.*, 2005]. A constant confining pressure (P_c) was achieved using silicone oil fed from a large-volume hydraulic pump coupled to a servo-controlled pressure intensifier. Acoustic emission (AE) output was monitored continuously during each experiment, primarily to aid determination of the onset of shear-enhanced compaction (C^*). AE was recorded via PZT-5A transducers (3 mm in diameter and 1 MHz longitudinal resonant frequency) mounted on steel inserts embedded within the nitrile sample jacket, and stored by a Vallen AMSY-5 acoustic emission acquisition system.

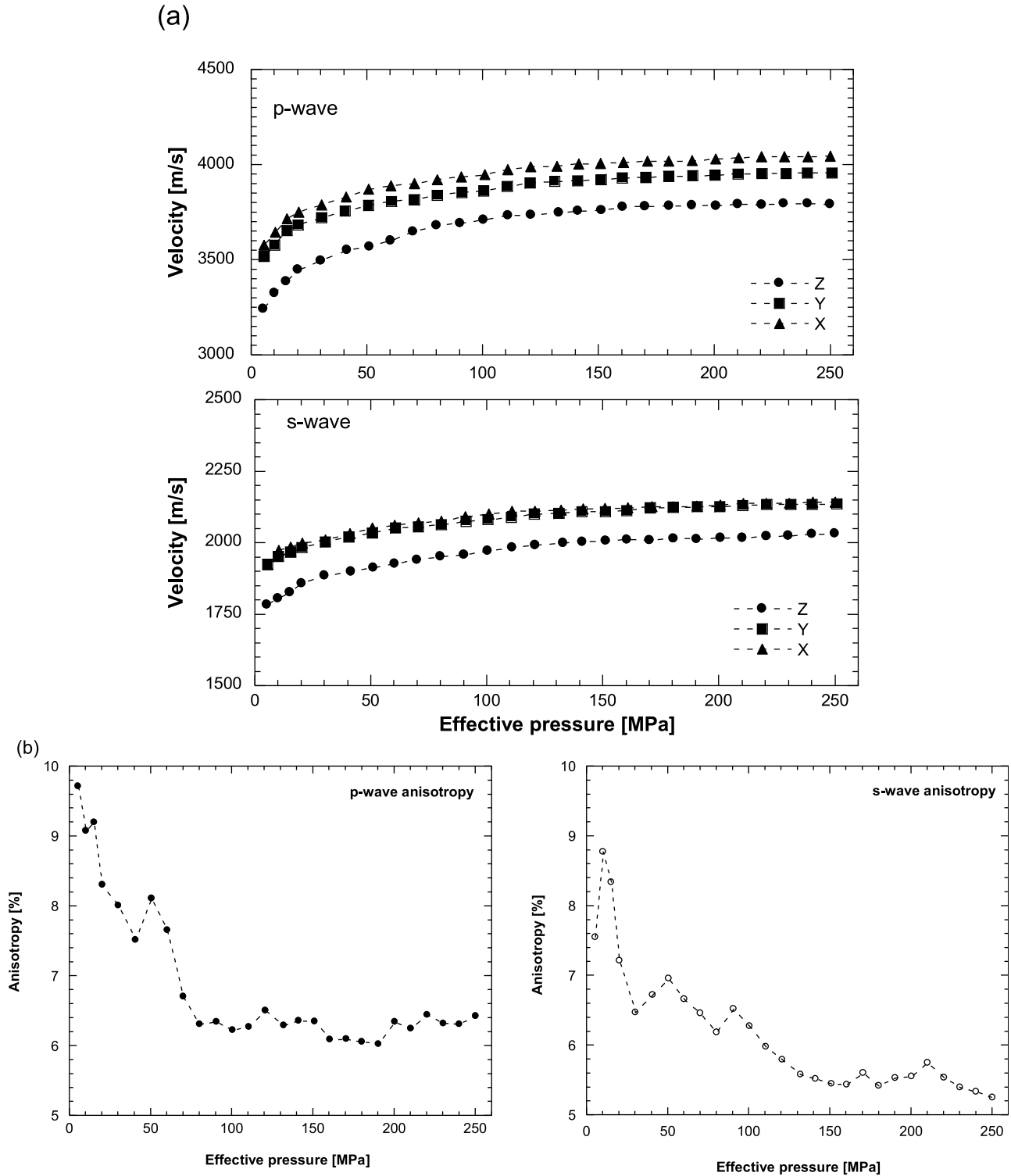


Figure 4. (a) Change in P and S-wave velocities as a function of effective pressure along the X, Y, and Z axes. (b) Variation in elastic wave velocity anisotropy as a function of hydrostatic pressure for P waves (left) and S waves (right).

[20] All triaxial deformation experiments were conducted at a servo-controlled constant strain rate of 10^{-5} s^{-1} . During some dedicated deformation experiments we also made sequential permeability measurements at increments of 0.25% axial strain using the steady state flow technique. In

these latter experiments it was necessary to stop the displacement of the loading ram so that any change in pore fluid flux measured by displacement of the pore fluid intensifiers could be attributed to the differential pore pressure applied across the sample and not to the action of the

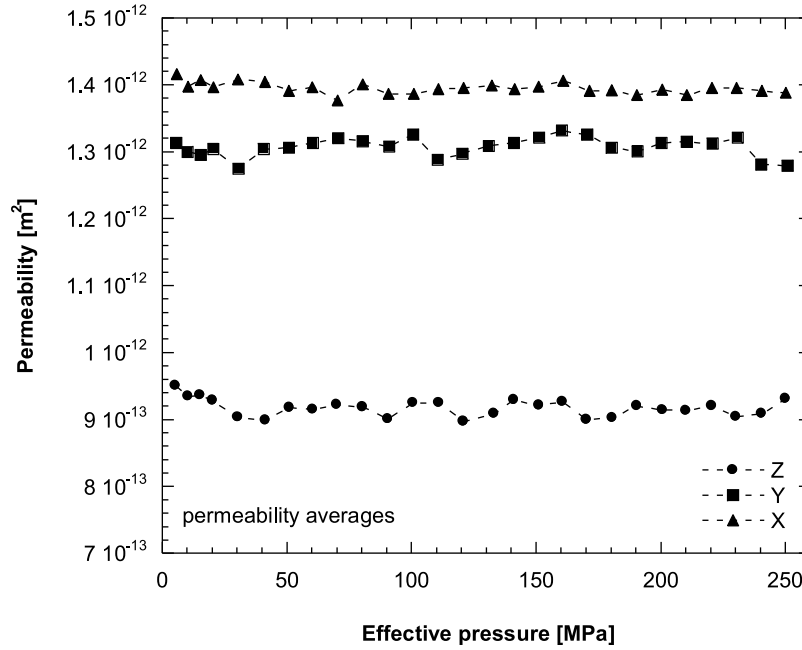


Figure 5. Change in permeability as a function of hydrostatic pressure for flow in the X, Y, and Z directions (average from 2 samples in each orientation). The pore fluid pressure was constant at 20 MPa for all measurements.

advancing ram forcing pore fluid from the sample as it deformed. Once the ram had been stopped, the system was allowed to equilibrate before a differential pore fluid pressure of 0.5 MPa was imposed across the sample by opening the previously isolated downstream intensifier in order to induce fluid flow. Displacement of the fluid intensifiers was then used to measure the volume flow as a function of time until steady state flow was established. Once the measurement was complete, the downstream intensifier was re-isolated, stopping flow, and the loading ram re-started. The sample was then allowed to deform by a further axial strain increment of 0.25% before the whole process was repeated for the subsequent permeability measurement. Permeability values were then calculated from the steady state fluid flow rate and the sample dimensions by simple application of Darcy's law.

4. Mechanical Data

[21] In this paper we use the convention that compressive stresses and compactive strains are positive. We will denote the maximum, intermediate and minimum principal stresses by σ_1 , σ_2 and σ_3 , respectively. The pore fluid pressure is denoted by P_p , and the difference $P_c - P_p$ between the confining pressure ($P_c = \sigma_2 = \sigma_3$) and the pore fluid pressure will be referred to as the "effective pressure" P_{eff} . The effective mean stress $(\sigma_1 + 2\sigma_3)/3 - P_p$ will be denoted by P and the differential stress $\sigma_1 - \sigma_3$ by Q .

[22] We first present new data on samples of Diemelstadt sandstone deformed normal (Z) and parallel (X) to bedding. Figure 6 summarizes the volumetric behavior of all the deformed samples. For reference, hydrostatic compaction tests were also performed in each of the two orientations, and the results of these tests are also plotted on Figure 6 as "hydrostats" for comparison with the triaxial data. The new

data exhibit similar patterns for both orientations, and are also similar to results reported in a number of previous studies on porosity change in sandstones [Wong et al., 1997; Baud et al., 2000, 2006]. The hydrostats essentially exhibit 3 phases: (1) a nonlinear phase at low pressure corresponding to the closure of pre-existing crack porosity, (2) a quasi-linear poroelastic phase, and (3) a significant deviation from linearity above a critical pressure P^* corresponding to the onset of grain crushing and pore-collapse. Beyond P^* the deformation is irreversible and the samples failed by homogeneous cataclastic compaction.

[23] Under triaxial loading at low effective pressures ($P_{eff} = 10$ MPa and 20 MPa) we observe deviations from the hydrostat above a critical stress C' , associated with volume dilatancy and shear faulting. At effective pressures of 40 MPa and beyond, we observe shear-enhanced compaction [Curran and Carroll, 1979; Wong et al., 1997] above a critical stress of C^* . Post-test visual inspection of the samples deformed at $P_{eff} = 40$ MPa revealed compaction bands in the Z sample and compactive shear bands in the X sample. At higher pressures, compaction bands were observed in all samples, regardless of orientation, in agreement with results reported in Townend et al. [2008] for measurements on the same material.

[24] In Figure 7 we show comparisons between the axial stress-strain curves and volume change data for both orientations from representative experiments performed at effective pressures of 10, 40 and 150 MPa. At $P_{eff} = 10$ MPa the stress-strain curves show typical brittle behavior with a peak stress followed by strain softening and failure on a macroscopic shear fault. The onset of both dilatancy and failure occurred at higher differential stress Q for the Z sample in agreement with previous studies that showed that porous sandstones are stronger when deformed normal to bedding in the brittle regime [Millien, 1993; Baud et al., 2005; Louis

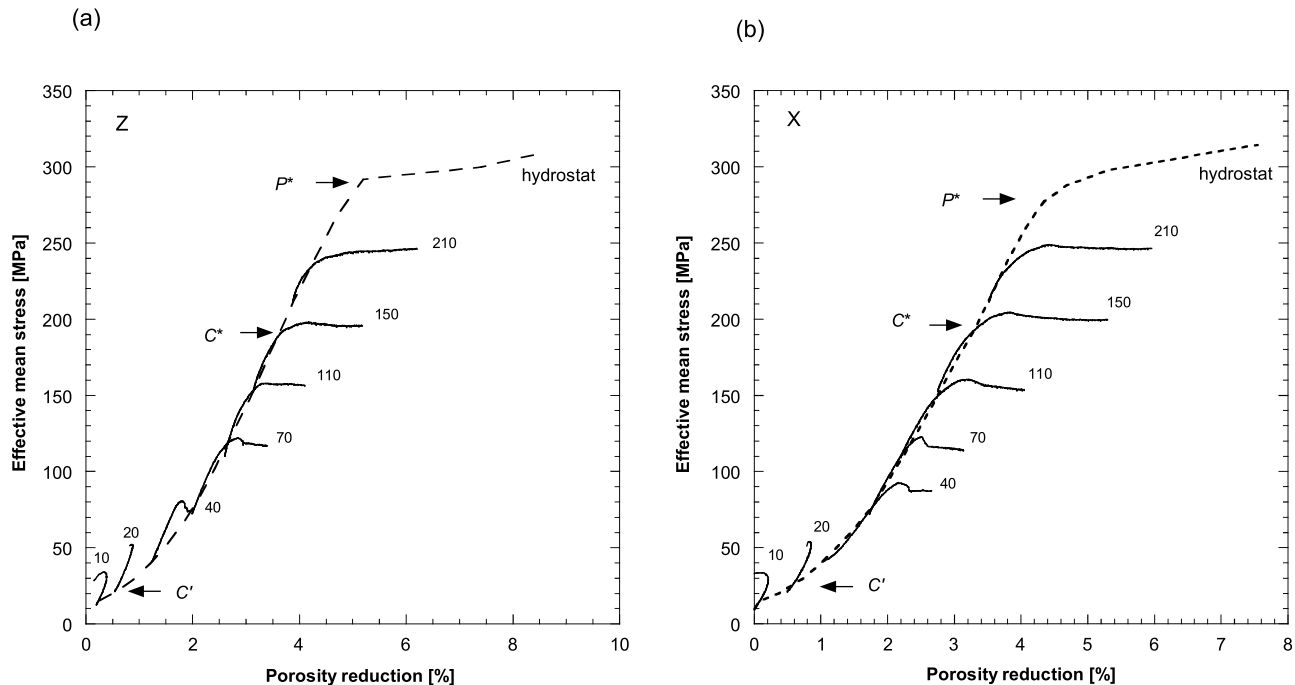


Figure 6. Plots of effective mean stress versus porosity reduction for triaxial compression experiments on Diemelstadt sandstone samples of (a) the Z series and (b) the X series. The effective pressures are indicated next to each curve (in MPa). For reference, the hydrostatic data are also shown as dashed lines. Arrows mark critical stress states P^* for hydrostatic experiments, C^* for the triaxial experiments at an effective pressure of 150 MPa, and C' for the triaxial experiments at an effective pressure of 20 MPa.

et al., 2009]. At $P_{eff} = 40$ MPa, the failure mode is different for both orientations, and is characterized by compactive rather than dilatant behavior. Here, the Z sample contains compaction bands and is significantly weaker than the X sample containing compactive shear bands. At all higher effective pressures, we observed that X samples were systematically stronger, and yielded at higher differential stresses, as shown in Figure 7c for the samples deformed at $P_{eff} = 150$ MPa.

[25] In Figure 8, we illustrate representative acoustic emission (AE) hit rate data for Z and X samples deformed in the compactive regime at the same effective pressure (110 MPa). For both orientations, we observe a distinct break in slope of the hit-rate curve at a strain of around 1.6%. This corresponds to the yield point on the stress-strain curve, and marks the onset of shear-enhanced compaction in the samples. Shear-enhanced compaction is accompanied by grain crushing and pore collapse, and these are the mechanisms responsible for the enhanced AE activity from this point. We therefore use this break in slope as an independent verification of the yield point (C^*) determined from the porosity reduction curves presented in Figure 6. A compilation of C^* values, determined in this way, is presented in Table 1. For the Z sample we observe episodic peaks in AE activity which, following previous studies [Baud *et al.*, 2004], we associate with the growth of discrete, tabular compaction bands. By contrast, for the X sample we observe a single, strong peak followed by an extended period of relatively high but uniform AE activity which we associate with the generation of more diffuse compactive damage.

[26] Figure 9 summarizes the mechanical data in P - Q space. Beyond the brittle-ductile transition, the onset of shear-enhanced compaction C^* occurred at systematically lower Q in Z samples than in X samples, and the difference in yield stress between the Z and X samples appears relatively constant for different effective pressures. The value of P^* was essentially the same for both orientations. This is entirely as expected for hydrostatic compaction of a homogenous material, and thus confirms that our Diemelstadt sandstone is homogeneous while also being structurally anisotropic (see Figure 1b). This also means that the yield caps shown in Figure 9 for the two orientations are non-parallel.

5. Permeability Data

[27] The focus of the study reported here is on deformation in the compactive regime. Accordingly, we performed 6 targeted deformation experiments in which we also measured permeability by the method described above. These experiments were conducted at effective pressures of 40, 110, and 150 MPa on both Z and X orientation samples. The full set of results, showing both permeability and differential stress plotted against axial strain, is collated in Figure 10 and also summarized in Table 2. First, we note that the values of permeability at the start of each deformation experiment are very similar at close to 10^{-12} m², regardless of effective pressure or sample orientation. This is entirely consistent with the hydrostatic permeability data reported in Figure 5. We also note that each permeability measurement made during the deformation experiments is

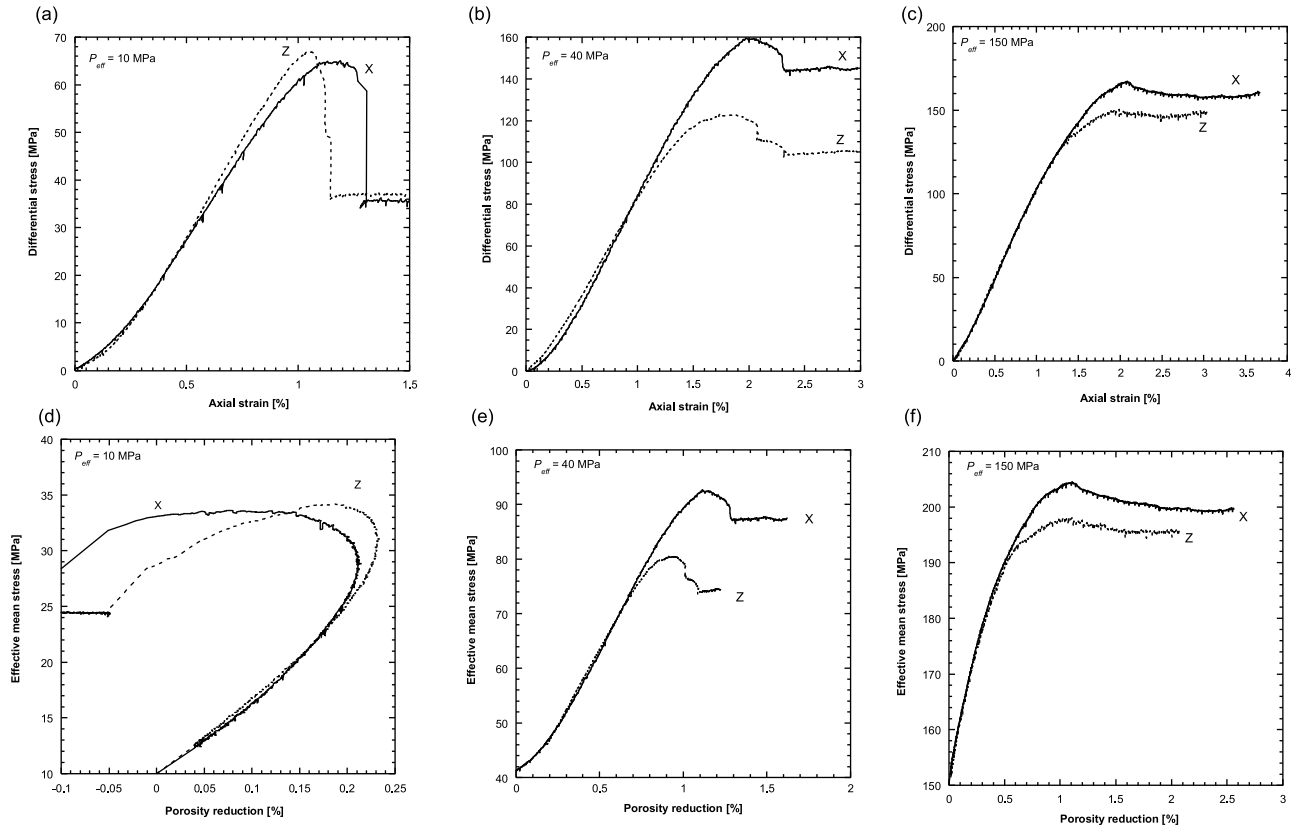


Figure 7. Selected mechanical data on Diemelstadt sandstone representative of the brittle faulting regime (Figures 7a and 7d), the transitional regime (Figures 7b and 7e), and the ductile regime (Figures 7c and 7f). Data are plotted both as (a–c) differential stress versus axial strain and (d–f) effective mean stress versus porosity reduction. The solid lines are for X samples and the dashed lines are for Z samples.

associated with a stress relaxation. This is a necessary consequence of stopping the loading ram to maintain constant strain and eliminate any extraneous fluid flux during the measurements. As expected, the stress relaxations are most marked at high differential stresses, as also reported by

Vajdova *et al.* [2004] for their measurements on Bentheim sandstone.

[28] In our data, we see a similar pattern of permeability evolution in Z samples at all effective pressures. A significant decrease in permeability is observed during initial

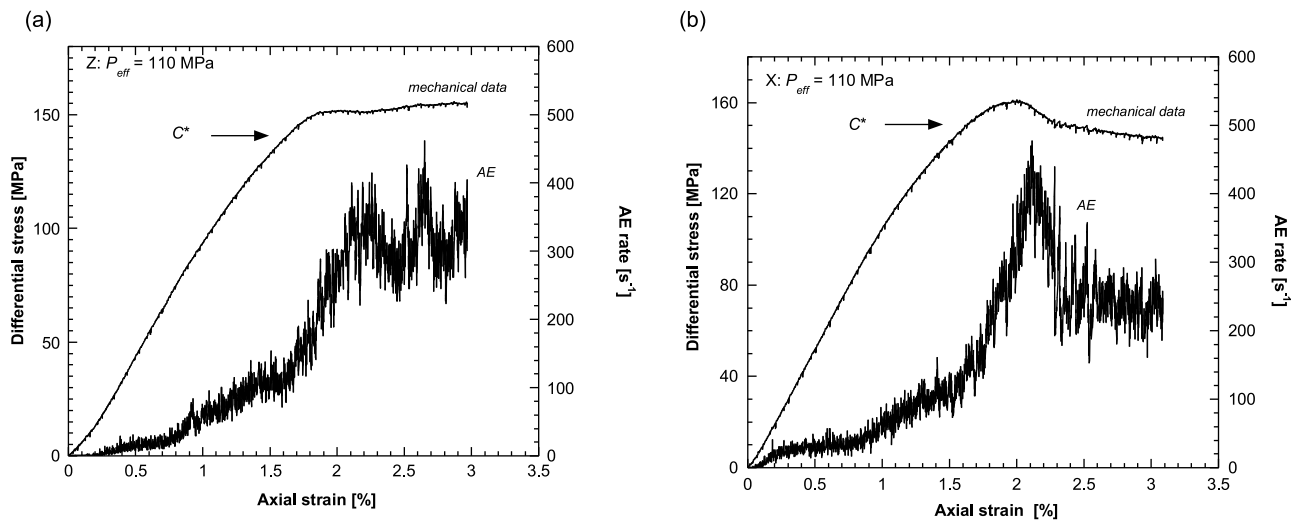


Figure 8. Differential stress and acoustic emission rate versus axial strain for triaxial experiments performed at an effective pressure 110 MPa on (a) a Z sample and (b) an X sample.

Table 1. Summary of Mechanical Data for Wet Diemelstadt Sandstone

Sample Orientation	Effective Pressure P_{eff} (MPa)	Critical Yield Stress (MPa)		Peak Stress (MPa)		Failure Mode
		Differential Stress	Effective Mean Stress	Differential Stress	Effective Mean Stress	
		$\sigma_1 - \sigma_3$	$(\sigma_1 + 2\sigma_3)/3 - P_P$	$\sigma_1 - \sigma_3$	$(\sigma_1 + 2\sigma_3)/3 - P_P$	
<i>Dilatant</i>						
X	10			65	33.6	dilatant shear band
X	20			101	54.2	dilatant shear band
Z	10			67	34.2	dilatant shear band
Z	20			95	51.9	dilatant shear band
<i>Compactant C*</i>						
X	40	140	86			compactive shear bands
X	70	152	120			discrete compaction bands
X	110	155	159			discrete compaction bands
X	150	146	198			discrete compaction bands
X	180	126	221			discrete compaction bands
X	210	103	243			discrete compaction bands
Z	40	117	79			mixed mode
Z	70	135	115			discrete compaction bands
Z	110	140	154			discrete compaction bands
Z	150	122	190			discrete compaction bands
Z	180	109	218			discrete compaction bands
Z	210	80	237			discrete compaction bands
<i>P*</i>						
X		0	280			distributed cataclasis
Z		0	283			distributed cataclasis

quasi-elastic loading; again consistent with similar decreases reported by *Vajdova et al.* [2004]. This is followed in each case by a large and rapid drop in permeability that occurs some time after the commencement of shear-enhanced

compaction at C^* , and that we associate with propagation of the first bedding-parallel CB. This time delay is entirely as expected, since CB growth is rather slow and we would not expect the dramatic drop in permeability to occur until the

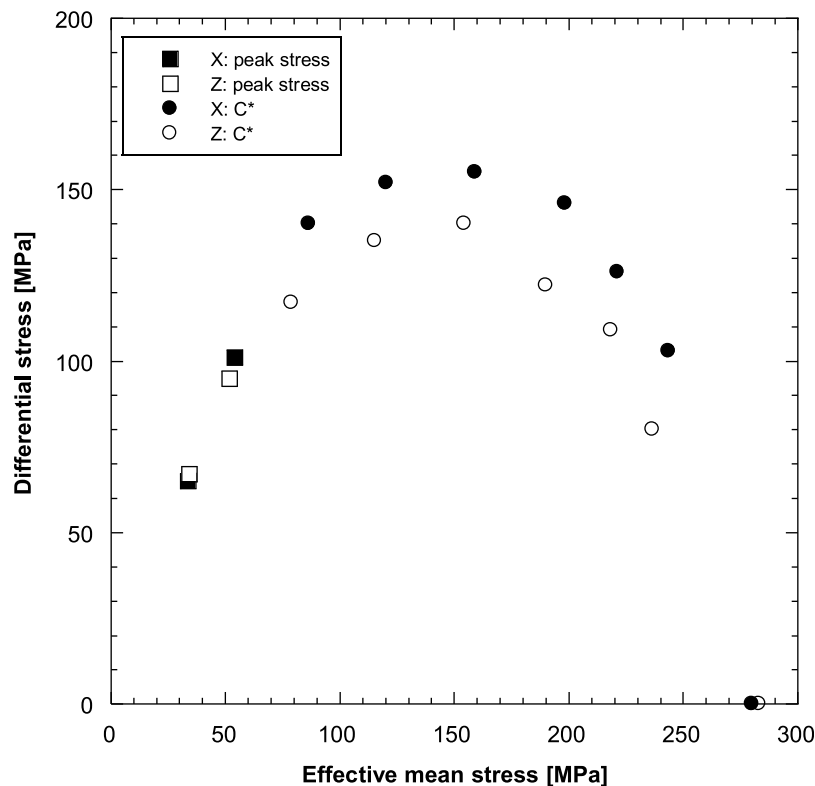


Figure 9. Strength envelopes for Diemelstadt sandstone in P - Q space described by peak stress (squares) for the brittle regime and critical yield stress C^* (circles) for the ductile regime. Solid symbols are for X samples and open symbols are for Z samples.

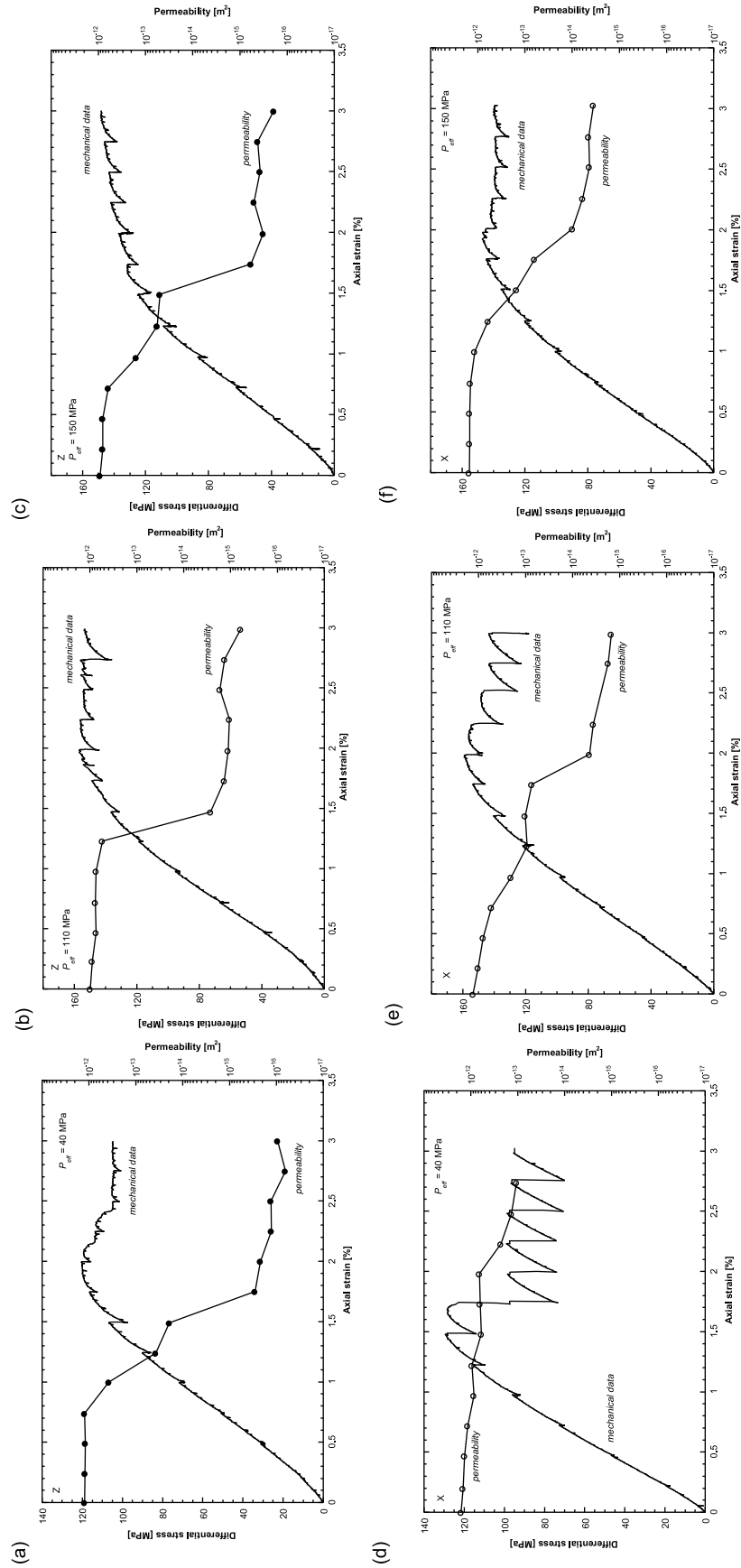


Figure 10. Differential stress and permeability as a function of axial strain for the triaxial permeability experiments performed on Diemelstadt sandstone samples in both (a–c) Z and (d–f) X orientations. The experiments were performed at effective pressures of 40 MPa (Figures 10a and 10d), 110 MPa (Figures 10b and 10e) and 150 MPa (Figures 10c and 10f).

Table 2. Triaxial Permeability Data

Differential Stress $\sigma_1 - \sigma_3$ (MPa)	Axial Strain (%)	Permeability ($\times 10^{-15} \text{ m}^2$)
<i>X: 40 MPa</i>		
0.0	0.00	1620
17.5	0.20	1480
46.7	0.47	1370
72.3	0.72	1160
95.7	0.97	865
115.4	1.22	940
123.4	1.36	750
128.2	1.48	592
103.5	1.73	629
97.3	1.98	661
98.9	2.23	231
97.5	2.48	136
96.4	2.74	107
<i>X: 110 MPa</i>		
0.0	0.00	1320.00
19.6	0.22	1030.00
45.2	0.47	802.00
72.6	0.72	535.00
98.1	0.97	202.00
121.8	1.23	92.00
140.4	1.48	100.00
145.8	1.60	90.00
153.8	1.74	74.00
149.8	1.99	4.40
153.3	2.24	3.60
124.9	2.75	1.75
143.4	2.99	1.49
<i>X: 150 MPa</i>		
0.00	0.00	1530.00
20.0	0.24	1480.00
47.8	0.49	1480.00
75.3	0.74	1450.00
100.0	1.00	1170.00
118.7	1.25	601.00
130.2	1.40	350.00
135.3	1.51	150.00
144.4	1.76	62.10
144.8	2.01	9.77
140.8	2.26	6.00
132.9	2.52	4.30
136.8	2.77	4.44
137.3	3.03	3.53
<i>Z: 40 MPa</i>		
0.0	0.00	1240.00
12.8	0.24	1210.00
30.7	0.49	1200.00
50.7	0.74	1240.00
70.4	1.00	374.00
90.2	1.24	37.70
103.7	1.44	20.00
106.6	1.49	19.30
113.4	1.75	0.29
116.4	2.00	0.22
110.2	2.25	0.13
102.3	2.50	0.13
104.3	2.75	0.06
105.0	3.00	0.09
<i>Z: 110 MPa</i>		
0.0	0.00	978.00
15.7	0.23	899.00
37.4	0.47	734.00
66.8	0.72	768.00
94.3	0.98	742.00
117.50	1.23	547.00
130.4	1.37	380.00
136.5	1.47	2.67

Table 2. (continued)

Differential Stress $\sigma_1 - \sigma_3$ (MPa)	Axial Strain (%)	Permeability ($\times 10^{-15} \text{ m}^2$)
148.8	1.73	1.37
156.5	1.98	1.12
148.5	2.24	1.07
149.4	2.49	1.69
146.2	2.74	1.34
153.3	2.99	0.69
<i>Z: 150 MPa</i>		
0.0	0.00	921.00
15.1	0.22	815.00
38.0	0.47	805.00
62.0	0.72	622.00
86.3	0.97	158.00
106.2	1.23	56.60
118.2	1.39	50.00
124.50	1.49	49.60
126.0	1.74	0.58
137.0	1.99	0.32
134.0	2.25	0.50
136.9	2.50	0.38
139.5	2.75	0.42
148.2	3.00	0.19

first CB had propagated across a significant proportion of the sample cross-section and become a well-developed barrier to fluid flow. *Townend et al.* [2008] calculated a propagation rate of 0.08 mm.s^{-1} for growth of the first bedding-parallel CB in samples of Diemelstadt sandstone from the same block deformed at the same rate. This means that it can take up to 500 s for the first CB to propagate across the whole sample cross-section, equivalent to a strain of up to 0.5% at a strain rate of 10^{-5} s^{-1} . Therefore, if the first CB nucleates at C^* , we would expect a strain offset of up to a maximum of 0.5% before we see the permeability drop, and that is what we observe for Z samples in Figure 10. In each case, the drop in bulk permeability is around 2 orders of magnitude. Although this first CB represents only a narrow zone embedded within the sample matrix, the overall sample permeability is essentially controlled by this low permeability band and this implies that the local permeability within the CB is at least 2 orders of magnitude lower than that of the matrix. Further strain, and the propagation of more CBs, then results in only relatively modest further decreases in permeability. Again, this is entirely as expected, since the first CB has already turned a high permeability rock sample into a low permeability one. Overall, sample permeabilities are reduced by between 3 and 4 orders of magnitude over the duration of the experiments.

[29] By contrast, we see a different pattern of permeability evolution in X samples. At 40 MPa, the X sample is some 10% stronger than the Z sample and deforms in the brittle faulting regime. Under these conditions, we do not propagate CBs and hence we observe only a relatively minor reduction in permeability by a little over one order of magnitude. At 110 and 150 MPa, we see overall permeability reductions of between 2 and 3 orders of magnitude. Not only are these reductions lower than for the Z samples, but the evolution is more gradual. We suggest that these differences in the evolution of permeability reduction are primarily related to the different distribution and less tabular nature of

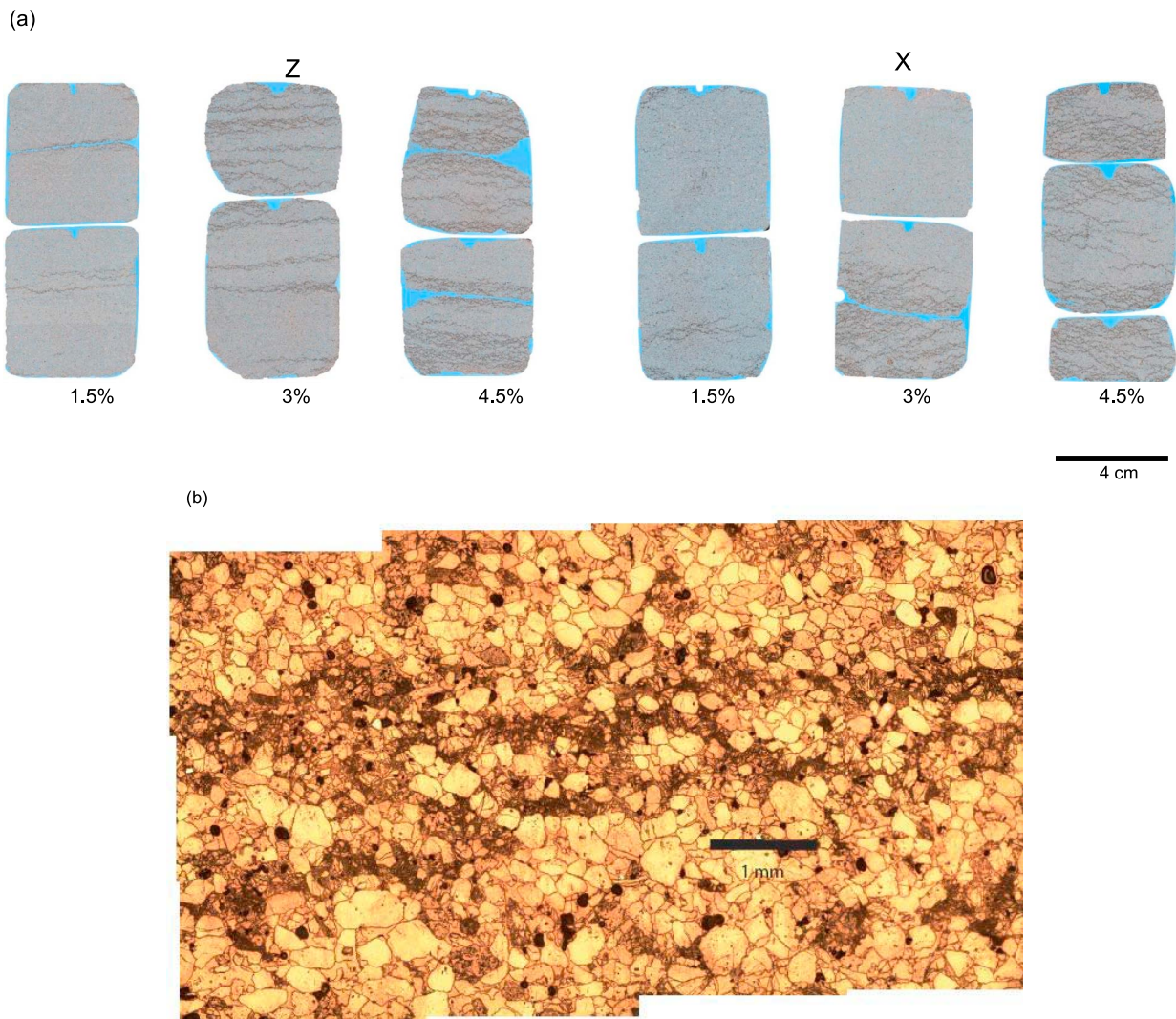


Figure 11. (a) Transmission optical micrographs of thin sections of Z and X samples of Diemelstadt sandstone deformed at an effective pressure of 150 MPa to different levels of axial strain: 1.5%, 3% and 4.5%. The dark bands are associated with significant local comminution. (b) Mosaic of micrographs showing the details of a compaction band in Diemelstadt sandstone. The maximum principal stress σ_1 was in the vertical direction.

CBs that are propagated in X samples, as discussed in the following section.

6. Microstructural Analysis of Deformed Samples

[30] As noted above, we observe somewhat different patterns of permeability reduction depending on effective pressure and sample orientation. In order to gain further insight into the parameters controlling these differences in permeability evolution, we performed an additional series of experiments specifically to study the microstructure of deformed samples. We investigated systematically the evolution of damage in both Z and X samples at $P_{eff} = 150$ MPa; a pressure that is well into the compactive regime for both orientations. Following the same procedure as reported in several previous studies [Menéndez *et al.*, 1996; Wu *et al.*, 2000; Baud *et al.*, 2004], we deformed three samples of each orientation to different levels of axial strain (1.5%,

3.0% and 4.5%). After being deformed, samples were slowly unloaded and then brought back to ambient pressure conditions. Petrographic thin sections were then prepared from samples that had been carefully removed from their rubber sleeves and dried before being impregnated with colored epoxy resin.

[31] Images of the full set of thin sections are presented in Figure 11a. Several important observations are worth noting. First, discrete compaction bands are the dominant feature of compactive deformation for both our Z and X orientation samples, in agreement with previously reported results for Diemelstadt sandstone by Tembe *et al.* [2008] and Townend *et al.* [2008]. The CBs propagate sequentially from different positions along the sample length with increasing strain until they eventually fill the whole sample volume. Second, we observe major differences between the spatial distribution and geometry of bands in the two orientations. CBs that propagate in Z samples appear tabular, parallel

or sub-parallel to the bedding plane, and cross the full diameter of the sample. By contrast, CBs in X samples appear shorter and more tortuous. They commonly propagate at oblique angles, and generally do not cross the full diameter of the sample. They also tend to commence growing close to the sample ends, as previously observed for CBs in Bentheim sandstone by *Vajdova et al.* [2004]. Figure 11b presents a mosaic of micrographs providing details of the microstructure of several CB segments in a Z sample. While considerable damage, in the form of grain comminution, is visible within the bands, no significant damage is visible outside the bands. The mean thickness of these bands is about $l = 650 \mu\text{m}$. Bands in X samples, although somewhat more tortuous, exhibit the same average thickness.

[32] We suggest that the contrasting microstructures explain well why the decreases in permeability observed in Z samples are significantly greater and more abrupt than those in X samples. Because X sample CBs grow at oblique angles and rarely cross the full sample diameter, they are less efficient at restricting fluid flow and it will therefore take more of them to provide an effective flow barrier.

7. Discussion

[33] Our microstructural and permeability data both suggest that the pre-existing structural anisotropy of Diemelstadt sandstone plays a key role in the development of compaction bands in samples deformed both normal and parallel to the bedding plane.

7.1. Discrete Compaction Bands in Diemelstadt Sandstone

7.1.1. Bedding Parallel Compaction Bands: Z Samples

[34] To infer the porosity and permeability reductions within the CBs in Z samples, we followed the approach used by *Vajdova et al.* [2004]: we first estimate the relation between the inelastic strain ϵ_p and the number of bands n . We define ϵ_p as the inelastic strain beyond the yield point C^* . We then estimate n by counting the number of intersections of CBs with an array of three axial scan-lines superimposed on the thin-section images (one in the center and one 5 mm from each edge); n is then simply taken as the arithmetic mean of the number of intersections with each scan-line. Figure 12a shows the number of bands as a function of inelastic strain for our three experiments performed in the Z direction. For comparison, the data of *Vajdova et al.* [2004] on Bentheim sandstone are also presented. We observe a significantly larger number of bands in our samples for the same amount of inelastic strain because our samples are significantly larger (more than $\times 5$ in volume). It should also be noted that the data of *Vajdova et al.* [2004] were compiled from samples deformed at different pressures, and this is probably why their data are significantly more scattered. Our data can be fitted with a straight line:

$$\epsilon_p = \epsilon_0 + \beta n \quad (1)$$

with $\epsilon_0 = 1.5 \times 10^{-5}$ and $\beta = 9.39 \times 10^{-4}$, where, ϵ_0 is the inelastic strain necessary to trigger the first band in the sample and β is the inelastic strain necessary to propagate each additional band. In agreement with previous studies [*Baud et al.*, 2004; *Vajdova et al.*, 2004], we found that the development of CBs occurred with negligible lateral

deformation. Also, since the differential stress changes very little during the phase of shear-enhanced compaction in our samples, we expect there to be little or no damage occurring outside the bands; as also confirmed from our microstructural observations. Under these conditions, the local porosity reduction within a compaction band β' can be estimated simply from the macroscopic inelastic strain β (taken over the full length of the sample = 100 mm) divided by the band thickness l : $\beta' = \Delta\phi = \Delta V/V = \Delta l/l = 9.39 \times 10^{-4} \times 100/0.650 = 0.144 = 14.4\%$. We observe that this calculated porosity reduction in the band is of the same order as values reported in previous studies by *Vajdova et al.* [2004] and *Louis et al.* [2006], who found 14% and 13.8%, respectively.

[35] As noted above, ϵ_0 was interpreted by *Vajdova et al.* [2004] as the inelastic strain necessary to trigger the development of the first CB beyond the yield point C^* . They suggested that some inelastic deformation was necessary before the development of the first CB in their samples. Although the nature of this inelastic deformation was not made clear, it is likely that it involved some cracking in the weaker part of the samples. By contrast, the observation that this factor is extremely small for our experiments suggests that the onset of bedding-parallel CB propagation is essentially concomitant with the yield point in our anisotropic Diemelstadt sandstone. Figure 12b shows the geometry considered by *Vajdova et al.* [2004] to interpret their permeability data (i.e., a porous material with n lower porosity horizontal CBs), modified to our sample dimensions. This also appears perfectly suitable for interpretation of our Z sample data. Using this geometry, the effective measured sample permeability k can be derived directly from Darcy's law and written as [*Freeze and Cherry*, 1979]

$$k = \frac{k_m}{\left(\frac{\epsilon_p}{\beta}\right)\left(\frac{k_m}{k_{cb}} - 1\right) + 1} \quad (2)$$

where k_m is the matrix permeability at C^* and k_{cb} is the permeability within a Z direction CB.

[36] In Figure 12c, we show that, when normalized to the matrix permeability, all our measured permeability data (k/k_m) can be bracketed within permeability contrast (k_m/k_{cb}) bounds of 1500 and 15000. For the experiment performed at 150 MPa, Figure 12d shows that the permeability data can be well fitted with a k_m/k_{cb} ratio of 2500. We note that, up to the formation of the first compaction band, the measured sample permeability k is equal to the matrix permeability k_m . For this experiment, the matrix permeability at C^* was therefore $k_m = 5 \times 10^{-14} \text{ m}^2$, which leads to $k_{cb} = 2 \times 10^{-17} \text{ m}^2$. Repeating the same analysis for our other two Z sample experiments gives values of $k_{cb} = 1 \times 10^{-17} \text{ m}^2$ for 40 MPa and $k_{cb} = 4 \times 10^{-17} \text{ m}^2$ for 110 MPa. Hence, we find that all of our calculated values of k_{cb} fall within the narrow range of 1 to $4 \times 10^{-17} \text{ m}^2$. This suggests that the permeability within compaction bands is essentially independent of pressure in a similar and consistent manner to the permeability of the sample matrix.

7.1.2. Bedding Oblique Compaction Bands; X Samples

[37] When observed locally under optical and scanning electron microscopy, the internal structure and thickness of compaction bands in X samples appears very similar to that

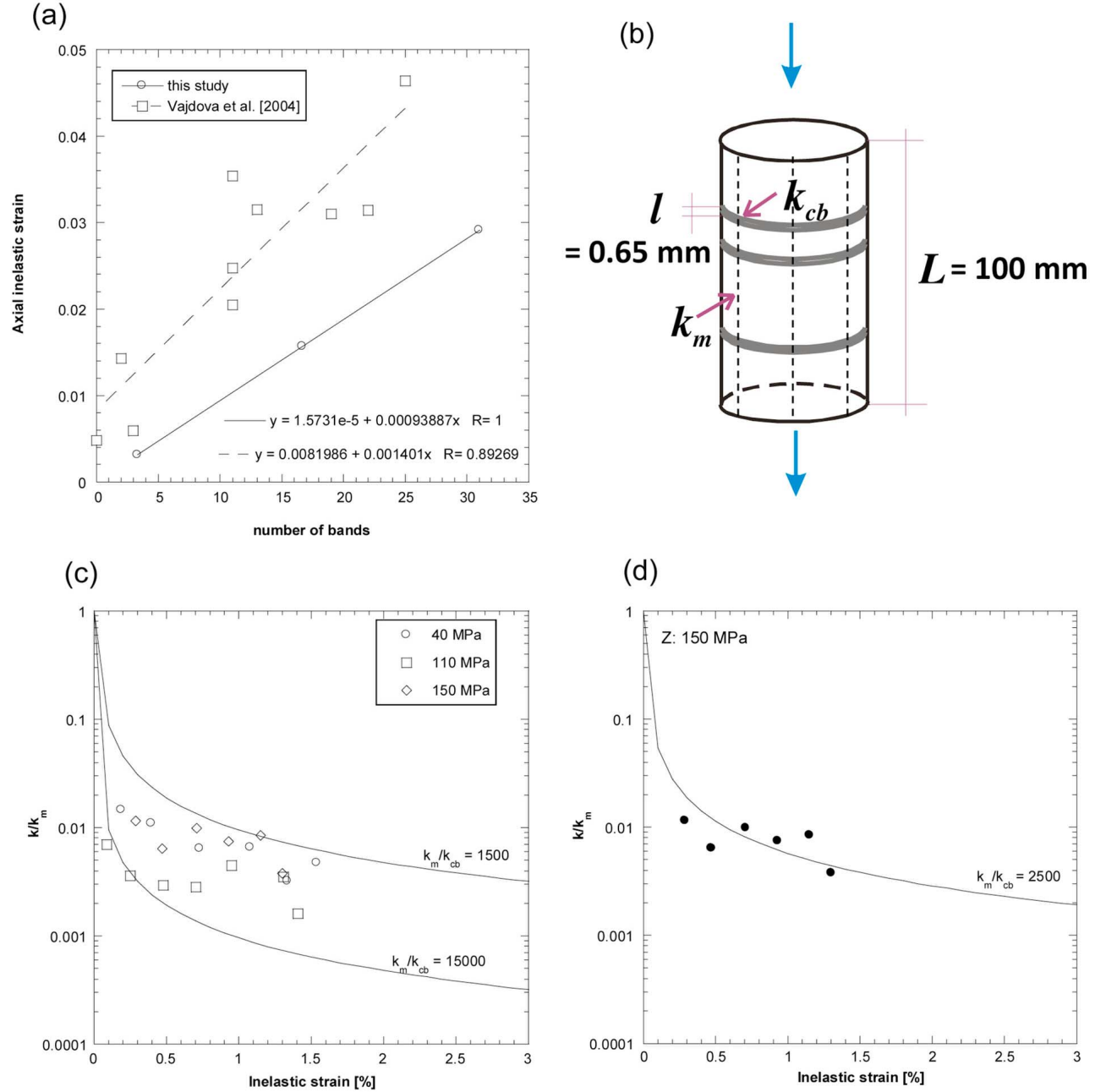


Figure 12. (a) Number of compaction bands as a function of axial inelastic strain for Z samples of Diemelstadt sandstone (circles) deformed at an effective pressure of 150 MPa. The data of Vajdova *et al.* [2004] for Bentheim sandstone (squares) are shown for comparison. The equations represent linear fits to the data. (b) Schematic representation of a Z sample in which compaction bands of permeability k_{cb} develop orthogonally to σ_1 in a material of bulk permeability k_m . The dashed lines represent the scan-lines used to count the number of bands. (c) Normalized permeability as a function of inelastic strain. Data points represent permeability measurements made on Z samples during shear-enhanced compaction in experiments performed at effective pressures of 40, 110 and 150 MPa. The solid lines represent the predictions of equation (2) for the permeability contrasts k_m/k_{cb} indicated. (d) Detailed fit to the data from the experiment performed at an effective pressure of 150 MPa.

seen in Z samples. There is therefore no reason why the porosity reduction should be different in X sample CBs. However, for the permeability reduction, the normalized permeabilities for the X series (Figure 13a) show a somewhat different evolution with inelastic strain.

[38] It is clear from Figure 11a that the accumulation of tortuous band segments in some areas of the deformed X samples does not allow for determination of n by the scan-line technique. It is also questionable whether the

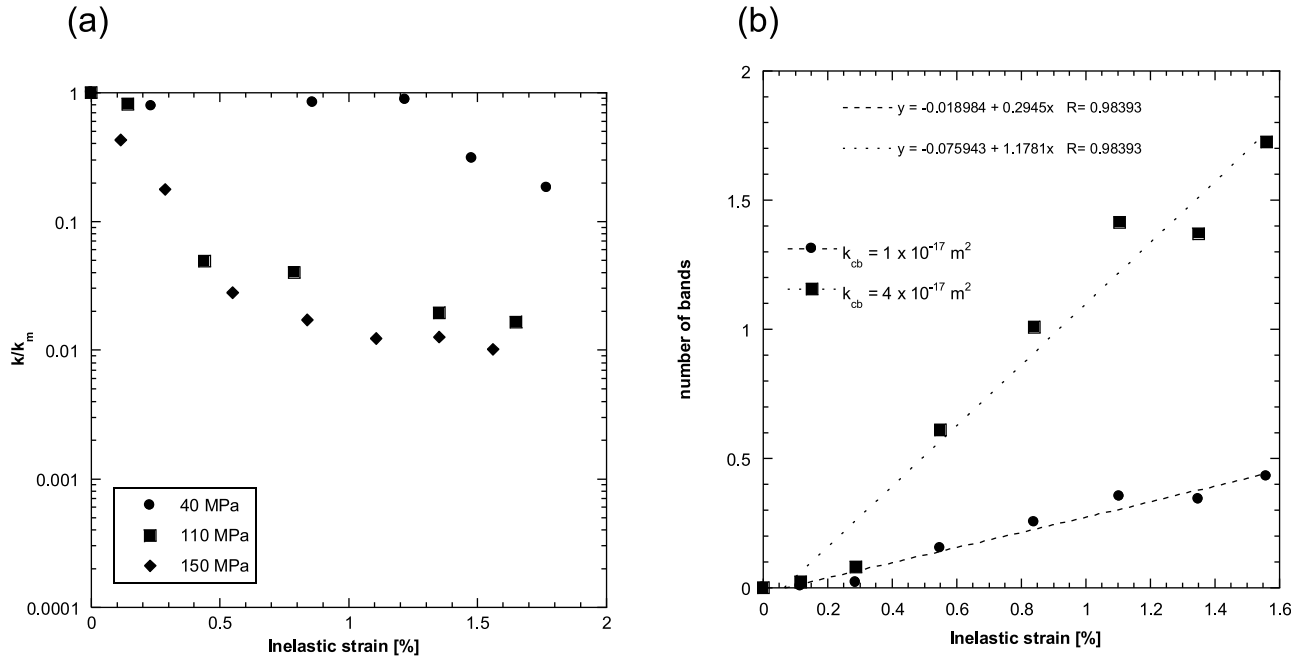


Figure 13. (a) Normalized permeability as a function of inelastic strain. Data points represent permeability measurements made on X samples during shear-enhanced compaction in experiments performed at effective pressures of 40, 110 and 150 MPa. (b) Predictions of equation (2) for the number of bands in the X sample deformed at an effective pressure of 150 MPa for $k_{cb} = 1 \times 10^{-17} \text{ m}^2$ (circles) and $k_{cb} = 4 \times 10^{-17} \text{ m}^2$ (squares).

geometry of Figure 12b is compatible with our thin-section observations (Figure 11a) and therefore appropriate for analysis of X sample data. To check this, we assume that β' is constant, as suggested by our microstructural observations, and solve equation (2) for n using the range of k_{cb} values that we calculated for the Z samples. Taking as one example the X sample deformed up to 3% axial strain, we obtain values for n that are less than 2 as shown in Figure 13b. This value is only about one tenth of that for the Z sample under the same conditions, and appears at first glance completely incompatible with the image of the X sample in Figure 11a. However, the analysis does provide us with a value for an “effective” number of bands and their influence on X-direction permeability. The result shows that the oblique band segments observed in X samples are not nearly as effective in reducing permeability as the more tabular and complete bands in Z samples. This further suggests that the 3D connectivity of CBs in X samples is very low and that this results in the observed lower and more gradual decrease of permeability measured in this orientation.

7.1.3. Comparison With CB Development in Other Sandstones

[39] The mechanical anisotropy observed in Diemelstadt sandstone in the brittle-faulting regime in this study is similar to that reported in previous studies on sandstone. The brittle strength is highest when the sandstone is deformed normal to bedding (Z) and lowest when deformed parallel to bedding (X). Unlike observations on shales and some foliated rocks, such as gneiss, which are weakest at some intermediate orientation [Rawlings *et al.*, 2002; Baud *et al.*, 2005], the brittle strength of Diemelstadt sandstone is expected to decrease monotonically between the Z and

X orientations [Millien, 1993; Bésuelle *et al.*, 2003; Louis *et al.*, 2009]. There is, however, a paucity of data describing the mechanical anisotropy of sandstone in the compactive regime. To our knowledge, the only systematic study is the recently published work of Louis *et al.* [2009] on Rothbach sandstone. We show their data in Figure 14a together with our new data on Diemelstadt sandstone. Louis *et al.* [2009] not only observed significantly larger mechanical anisotropy in their Rothbach sandstone, but they also found that their samples deformed normal to bedding (Z) were always significantly stronger than those deformed parallel to bedding (X). This is in complete contrast to our observations on Diemelstadt sandstone and also to what is predicted by models for composite materials with strong layers bonded to a relatively weak matrix [Hull, 1981]. However, for materials with complex microstructures, such as rocks, it is possible for either orientation to be either weaker or stronger depending on the microstructural geometry (grain shape, grain contact length, etc...). Acoustic emission location data for both Z and X samples of Diemelstadt sandstone [Townend, 2007; Townend *et al.*, 2008] showed that CB propagation commenced at the yield point in both cases, and our new permeability data also support this suggestion.

[40] Tembe *et al.* [2008] compiled data on the geometric attributes of both field and laboratory CBs, and used an anti-dislocation/anti-crack fracture mechanics model [Rudnicki, 2007] to obtain a scaling relation in which the stress level required for compaction band nucleation σ_{cb} is inversely proportional to the CB thickness l :

$$\sigma_{cb} = \frac{2G_c}{\pi\beta'l} \quad (3)$$

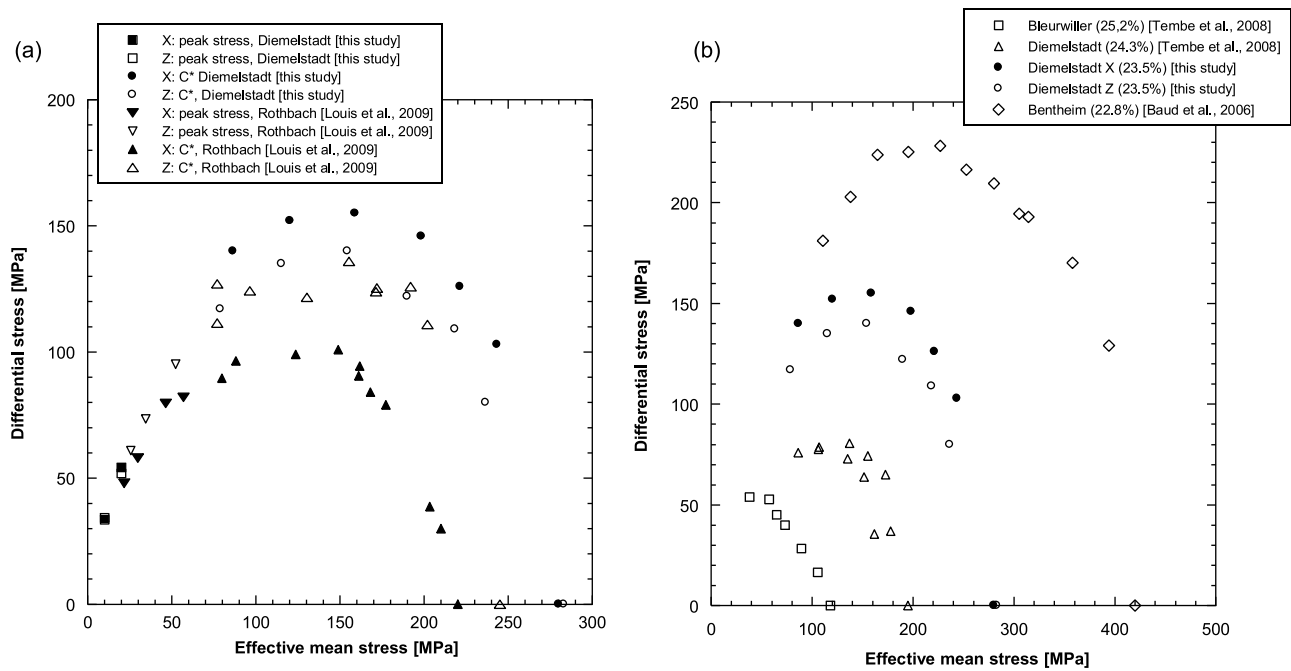


Figure 14. (a) Strength envelopes in P - Q space described by peak stress and critical yield stress C^* for Diemelstadt sandstone (this study) and Rothbach sandstone [Louis et al., 2009]. Closed symbols are for X samples and open symbols are for Z samples. (b) Critical yield stress C^* values in P - Q space for rocks in which compaction bands were observed in laboratory deformed samples: data from this study on Diemelstadt sandstone (open and solid circles for Z and X orientations, respectively), data from Tembe et al. [2008] on Diemelstadt (open triangles) and Bleurwiller (open squares) sandstones, and data from Baud et al. [2006] on Bentheim sandstone (open diamonds).

where β' is the porosity reduction in the band as described above and G_c is the fracture energy of the rock that needs to be overcome to enable band formation.

[41] Assuming that the shear-enhanced compaction commenced at the observed value of C^* for each orientation, our mechanical data lead to an average stress ratio of $\sigma_{cb}^Z/\sigma_{cb}^X = 0.93$. Figure 9 shows that this ratio remains essentially constant for all pressure conditions. Our microstructural observations also suggest that the CBs have essentially the same thickness and porosity reduction in both X and Z directions. Hence, the model of Tembe et al. [2008] suggests that the mechanical strength anisotropy observed in the compactant regime in Diemelstadt sandstone is primarily due to some moderate anisotropy in the fracture energy G_c required to propagate CBs parallel and normal to bedding; that is, $G_c^Z/G_c^X = 0.93$. There is a severe paucity of data on the anisotropy of fracture energy (G_c) or fracture toughness (K_c) in layered rocks, but Walters [1984] showed that the cleavage-normal fracture toughness of slate was nearly twice the cleavage-parallel value. Since $G_c \propto K_c^2/E$ (where E is Young's modulus), we might expect the cleavage-normal G_c to be 4 times greater than the cleavage-parallel G_c . However, the value of E is also anisotropic in this material, being as much as 3 times higher in the cleavage-normal direction. Our estimate of fracture energy anisotropy for Diemelstadt sandstone is therefore entirely consistent with Walters [1984] observations on slate. Further, Walters [1984] noted that when he attempted to propagate fractures normal or oblique to the isotropy plane, they commonly re-oriented in an attempt to propagate

along the lower-energy cleavage-parallel orientation. This is consistent with our microstructural observations of CBs propagating in an overall oblique orientation, made up of bedding-normal and bedding-parallel segments, when loaded in the bedding-parallel (X) direction.

[42] Bifurcation analysis [Rudnicki and Rice, 1975] potentially provides an alternative framework to study the occurrence of compaction localization. Rudnicki [2002] derived an analytical condition for the nucleation of CBs in a transversely isotropic material. However, the parameters used in his model are not accessible from conventional triaxial experiments. Specific, focused experiments would be required to ascertain if his model were in agreement with our experimental data and if it were able to predict the observed mechanical anisotropy in Diemelstadt sandstone; and this is beyond the scope of the current study.

[43] To date, discrete CBs have been observed in laboratory samples of Bentheim [Klein et al., 2001; Baud et al., 2004], Diemelstadt [Tembe et al., 2008; Townend et al., 2008] and Bleurwiller [Fortin et al., 2005; Tembe et al., 2008] sandstones. In all cases, the samples were deformed normal to the sedimentary bedding (our Z orientation). Although these rocks only cover a very narrow range of porosities (22.8–25.2%), they nevertheless cover a very wide range of strengths [Tembe et al., 2008]. We have compiled the compactive yield caps for all those rocks in which CBs were observed in Figure 14b. It is clear that compactive strength decreases dramatically with increasing porosity. For example, our samples of Diemelstadt sandstone with a porosity of 23.5% are significantly stronger than those of Tembe et al.

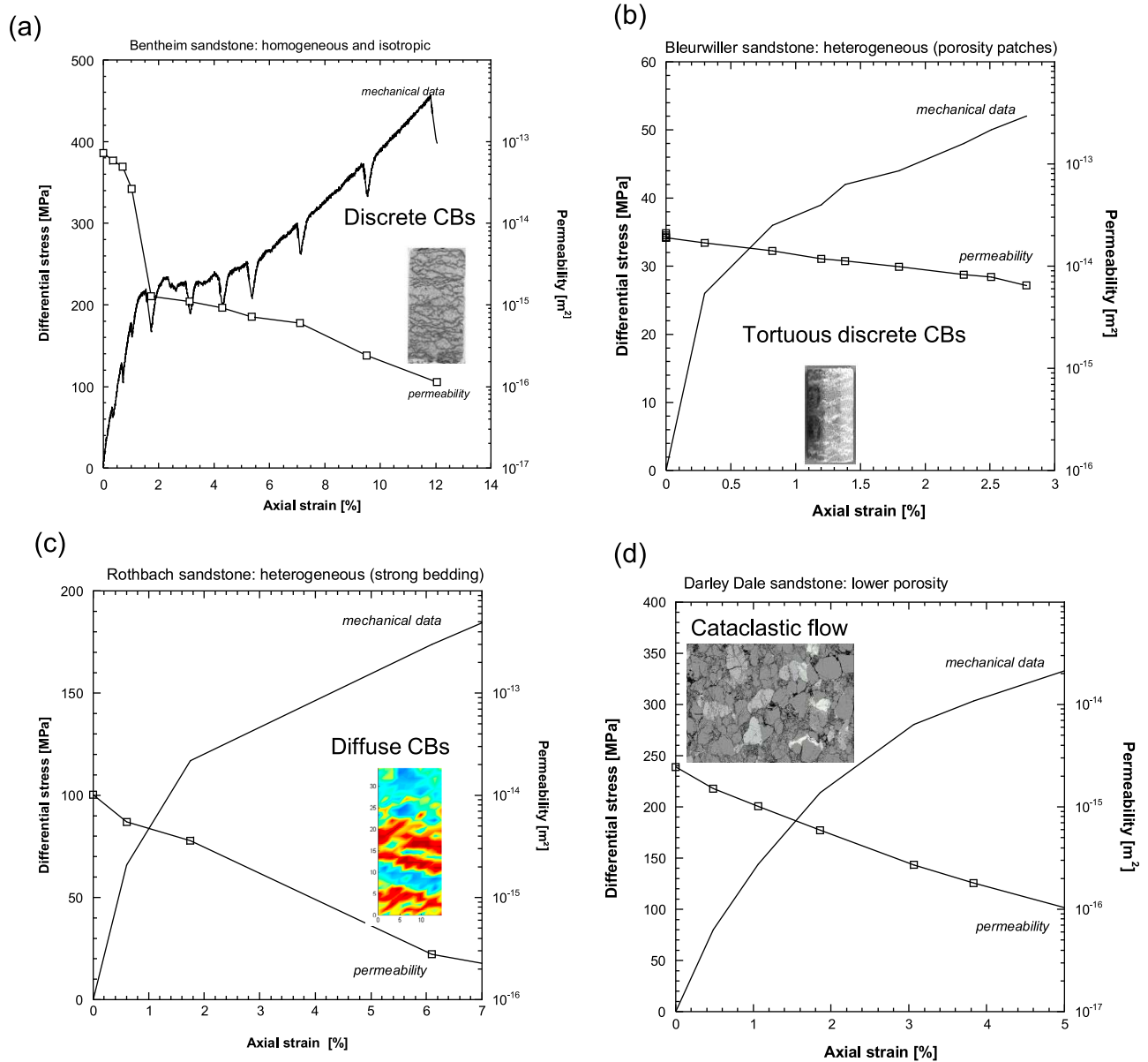


Figure 15. Differential stress and permeability versus axial strain for samples of (a) Bentheim sandstone deformed at an effective pressure of 300 MPa [Vajdova *et al.*, 2004], (b) Bleurwiller sandstone deformed at an effective pressure of 100 MPa [Fortin *et al.*, 2005], (c) Rothbach sandstone deformed at an effective pressure of 130 MPa [Zhu and Wong, 1997], and (d) Darley Dale sandstone deformed at an effective pressure of 200 MPa [Zhu and Wong, 1997]. Micrographs showing the failure mode for each case are given on each figure. The micrographs for Bleurwiller, Rothbach, and Darley Dale were presented by Baud *et al.* [2006], Bésuelle *et al.* [2003], and Wu *et al.* [2000], respectively.

[2008] with a porosity of 24.3%. The critical pressure for the onset of grain crushing and pore collapse P^* for our samples was 290 MPa, whereas that reported by Tembe *et al.* [2008] was 195 MPa. Zhang *et al.* [1990] proposed a Hertzian fracture model to describe grain crushing in which P^* should follow the trend $P^* \propto (\phi R)^{-3/2}$ where ϕ is the porosity and R is the grain size. Taking the characteristics of both rocks, the Zhang *et al.* model predicts that our samples should be only about 5% stronger than those of Tembe *et al.* [2008], so that the differences seen in Figure 14b cannot therefore be explained simply as due to

the combined effect of porosity and grain size. These differences most likely reflect the variable composition of Diemelstadt sandstone. A significantly larger proportion of weaker minerals such as feldspar were present in the material used by Tembe *et al.* [2008]. This likely caused their samples not only to be mechanically weaker but also to be significantly weakened by the chemical effect of water. It is also worth noting that the variability in the strength of Tembe *et al.*'s [2008] samples is broadly comparable with the difference in strength that we observe between our Z and X samples.

7.2. Influence of Compaction Localization on Permeability in Porous Sandstone

[44] One common attribute between all previous studies of CBs and our new results is that the porosity reduction in the bands, inferred from a variety of different methods (e.g., CT scanning, AE measurements, microstructural analysis), always appears to be in the range 14–15%. This suggests that the structures produced in laboratory experiments are essentially of the same nature whatever the rock type. Their impact on permeability is however quite different. This is illustrated in Figure 15, where we have compiled previously published permeability data on Bentheim [Vajdova *et al.*, 2004] (Figure 15a) and Bleurwiller [Fortin *et al.*, 2005] (Figure 15b) sandstone, where discrete compaction bands were reported, and, for comparison, data in Rothbach (Figure 15c) and Darley Dale (Figure 15d) sandstone [Zhu *et al.*, 1997] where diffuse compaction bands and homogeneous cataclasis were reported, respectively. We choose here to present data for different pressure conditions that corresponded to approximately the same portion of the compactant failure envelope for each rock. This compilation, taken together with our new data on Diemelstadt sandstone, suggests that permeability evolution during compactive deformation is controlled essentially by the degree of heterogeneity and anisotropy of the starting material which, in turn, controls deformation band nucleation and geometry.

[45] Previous studies based on CT scanning [Louis *et al.*, 2009], network modeling [Katsman *et al.*, 2005] and Discrete Element modeling [Wang *et al.*, 2008] suggested that the development of CBs was likely to be enhanced in more homogeneous rocks relative to more heterogeneous rocks. Bentheim and Diemelstadt sandstones are both relatively homogeneous, while Rothbach, Bleurwiller and Darley Dale sandstones exhibit a larger degree of heterogeneity associated with their sedimentary bedding [Bésuelle *et al.*, 2003], porosity variability [Fortin *et al.*, 2006] and more complex mineralogy and wider grain size distribution, respectively. Our permeability and microstructural data suggest that, for the homogeneous end-members (Bentheim and Diemelstadt), the anisotropy of the sandstone had a strong influence on strength and CB development. In our Z samples, sub-horizontal, sample-crossing bands nucleated from the yield point and created very efficient barriers to fluid flow. The permeability contrast between CB and matrix of 3 orders magnitude that we obtained is likely an upper bound to the effect of CBs in laboratory samples. In the X direction, shorter, more tortuous bands were less well connected and thus had a less dramatic influence on permeability. Vajdova *et al.* [2004] reported a large but less dramatic permeability contrast of two orders of magnitude in Bentheim sandstone which can probably be considered as an intermediate case between X and Z. The crucial role of 3D connectivity was also stressed recently by Pons *et al.* [2011], who found a permeability contrast of only a factor of 3 between a CB and the host rock in a sample of Bentheim sandstone. This is not surprising because their AE data and X-ray images suggest that their CB did not occupy the entire specimen cross-section.

[46] The presence of heterogeneities, such as the variable porosity patches reported by Fortin *et al.* [2006] for their Bleurwiller sandstone samples, appears to have a major

influence on the geometric attributes of CBs, leading to increased tortuosity, shorter length and much reduced effectiveness as permeability barriers. Comparing Figures 15b and 15d, it is clear that whether the compaction is localized or distributed has very little influence on the permeability evolution. This also appears to be the case in the presence of strong sedimentary bedding, such as in Rothbach sandstone (Figure 15c), where compaction occurs primarily in the higher porosity layers [Louis *et al.*, 2009].

7.3. Comparison With Bedding Parallel and Bedding Oblique Compaction Bands in the Field

[47] We have shown that CBs can develop oblique to the bedding plane in laboratory samples. This is entirely consistent with field observations, where the majority of reports show compaction bands at high angles to bedding; first in the Aztec sandstone (Nevada) by Hill [1989] and later in the Navajo sandstone (Arizona) by Mollema and Antonellini [1996]. More recently, Eichhubl *et al.* [2010] performed a systematic field analysis in the Aztec sandstone formation and distinguished two types of CBs: Pure CBs with only compactant deformation and what they termed shear-enhanced CBs that accommodated roughly equal amounts of shear displacement and band-perpendicular compaction by grain rearrangement and porosity collapse. Note that shear-enhancement is used purely in a kinematic sense rather than in a mechanical sense by Eichhubl *et al.* [2010]. The pure CBs observed by Eichhubl *et al.* [2010] develop across the bedding and are typically wavy and non-planar, so they are in many ways comparable to the CBs we observe in our X samples.

[48] Our new results also suggest that CBs are more likely to form and create efficient permeability barrier when they grow in the bedding plane. Aydin and Ahmadov [2009] recently reported observations of bedding-parallel CBs in Nevada. They suggested that earlier studies may not have reported CBs in such orientations simply because bedding-parallel compaction bands are more difficult to identify in the field where they can look like thin depositional layers. Furthermore, they might be disguised by later overprinting due to continued compaction, cementation and deformation [Eichhubl *et al.*, 2010].

[49] Aydin and Ahmadov [2009] report a porosity reduction of 13% in the field CBs which compares very well with the value we obtain for our laboratory samples and with previously reported values from laboratory [Baud *et al.*, 2004; Fortin *et al.*, 2006] and field [Mollema and Antonellini, 1996; Sternlof *et al.*, 2005] studies. The permeability contrast has not to date been directly measured on any field samples, but has been estimated in several pilot studies using the Lattice-Boltzman method applied to photomicrographs [Keehm *et al.*, 2006; Aydin and Ahmadov, 2009] and high-resolution X-ray microtomography images [Sun *et al.*, 2011]. There appears to be no consistent pattern in these reported results. While Aydin and Ahmadov [2009] and Sun *et al.* [2011] both estimated a permeability reduction of about a factor 6 between matrix and CB, Keehm *et al.* [2006] inferred a permeability contrast of up to 2 orders of magnitude. Part of the discrepancy between Sun *et al.* [2011] and Keehm *et al.* [2006] may be that the latter used 3D reconstruction of 2D data. More recently, Fossen *et al.* [2011] inferred a permeability contrast in the range

1 to 4 orders of magnitude by applying a modified version of the Kozeny-Carman relation [Torabi *et al.*, 2008] to photomicrographs of CBs in the field. Taken together, these field data therefore bracket the permeability contrasts we estimate from our laboratory measurements on Diemelstadt sandstone. However, Sternlof *et al.* [2005] point out that CBs generated in the laboratory are characterized by spectacular amounts of cataclasis, whereas those occurring in the field generally contain only minor amounts of cracking. Tembe *et al.* [2008] explained this apparent discrepancy on the basis of their model (equation (3)) which predicts that a much lower stress is required to propagate CBs in the field than in the laboratory. Such lower stresses are likely to produce less cataclasis, especially at the much lower strain rates expected for natural rock deformation. It is therefore unlikely that permeabilities in laboratory CBs will directly match those in natural CBs. However, the accuracy of the numerical simulations used to infer the permeability contrast in natural CBs hinges on a very precise 3D reconstruction of the pore-space from 2D images which is difficult to achieve at a representative scale. Direct permeability measurements on field samples hosting natural CBs are therefore clearly needed for comparison with laboratory measurements and to confirm or deny these suggestions.

[50] We have shown that CBs that propagate in the bedding plane are more tabular and less tortuous than those propagating oblique to bedding. Although Sternlof *et al.* [2005] and Aydin and Ahmadov [2009] studied, respectively, both types of band in the same area of the Aztec sandstone formation, there is still a paucity of field data which would enable us to compare the geometric attributes of CBs developing in both orientations. Again, direct measurement of permeability on the various types of natural structure is the logical next step suggested by our laboratory observations.

8. Conclusion

[51] In this paper, we have shown for the first time laboratory evidence for CBs developing in samples loaded both normal and parallel to bedding, and that this produces CBs parallel and oblique to bedding, respectively. The observation that bedding-parallel loading produces CBs oblique to bedding rather than normal to bedding suggests that it may be possible for CBs to develop in any intermediate orientation, but this will need to be confirmed by further detailed investigation. We have further shown that the pre-existing structural anisotropy of Diemelstadt sandstone resulted in the following:

[52] 1. A significant mechanical anisotropy with samples deformed parallel to bedding always stronger in the compaction regime. This mechanical anisotropy was interpreted as directly linked to the nucleation of CBs which was easier in the bedding-parallel direction.

[53] 2. Significant differences in the sequence of development of CBs in each orientation and in some of the geometric attributes of CBs. CBs developing in the bedding-parallel plane are tabular and only weakly tortuous, while CBs developing oblique to bedding are shorter, less tabular and significantly more tortuous.

[54] Consequently, CBs that propagate in the bedding-parallel direction have a much more significant impact on

permeability. Comparison of our new permeability data with previously published data on sandstone revealed that the effect of CBs on permeability is, to first order, a function of CB connectivity. The data further suggest that the largest effect is likely to be observed in anisotropic sandstones when tabular CBs grow in the bedding plane.

[55] In the field, CBs have been observed to occur in a variety of orientations relative to bedding planes. Further work is needed to map their geometric attributes as a function of their angle to bedding for comparison with the laboratory results. Direct measurements of permeability on field samples hosting natural CBs are also needed for comparison with laboratory measurements.

[56] **Acknowledgments.** We thank Steve Boon and Neil Hughes for technical assistance and Fabrice Surma for helping to collect the blocks of Diemelstadt sandstone. We have benefited from discussions with Mike Heap, Nicolas Lenoir, Laurent Louis, Sergio Vinciguerra, Sheryl Tembe, and Teng-fong Wong. We are grateful to Joel Sarout and one anonymous reviewer for thoughtful reviews. Our CT images of Diemelstadt sandstone were acquired by Jessie Maisano at University of Texas at Austin. This work was partially funded by a Royal Society/CNRS scientific exchange award to P.G.M. and P.B. (contract 17338).

References

- Aydin, A., and R. Ahmadov (2009), Bed-parallel compaction bands in Aeolian sandstone: Their identification, characterization and implications, *Tectonophysics*, 479, 277–284, doi:10.1016/j.tecto.2009.08.033.
- Baud, P., W. Zhu, and T. Wong (2000), Failure mode and weakening effect of water on sandstone, *J. Geophys. Res.*, 105, 16,371–16,389, doi:10.1029/2000JB900087.
- Baud, P., E. Klein, and T. Wong (2004), Compaction localization in porous sandstones: Spatial evolution of damage and acoustic emission activity, *J. Struct. Geol.*, 26, 603–624, doi:10.1016/j.jsg.2003.09.002.
- Baud, P., L. Louis, C. David, G. Rawlings, and T. Wong (2005), Effects of beddings and foliation on mechanical anisotropy and failure mode, *Geol. Soc. Spec. Publ.*, 245, 223–249, doi:10.1144/GSL.SP.2005.245.01.11.
- Baud, P., V. Vajdova, and T. Wong (2006), Shear-enhanced compaction and strain localization: Mechanical data and constitutive parameters for porous sandstones, *J. Geophys. Res.*, 111, B12401, doi:10.1029/2005JB004101.
- Benson, P. M., P. G. Meredith, and E. S. Platzman (2003), Relating pore fabric geometry to acoustic and permeability anisotropy in Crab Orchard Sandstone: A laboratory study using magnetic ferrofluid, *Geophys. Res. Lett.*, 30(19), 1976, doi:10.1029/2003GL017929.
- Benson, P. M., P. G. Meredith, E. S. Platzman, and R. E. White (2005), Pore fabric shape anisotropy in porous sandstones and its relation to elastic wave velocity and permeability anisotropy under hydrostatic pressure, *Int. J. Rock Mech. Min. Sci.*, 42, 890–899, doi:10.1016/j.ijrmms.2005.05.003.
- Bésuelle, P., P. Baud, and T. Wong (2003), Failure mode and spatial distribution of damage in Rothbach sandstone in the brittle-ductile transition, *Pure Appl. Geophys.*, 160, 851–868, doi:10.1007/PL00012569.
- Borja, R. I., and A. Aydin (2004), Computational modeling of deformation bands in granular media, I. Geological and mathematical framework, *Comput. Methods Appl. Mech. Eng.*, 193, 2667–2698, doi:10.1016/j.cma.2003.09.019.
- Boutéca, M. J., J.-P. Sarda, and O. Vincke (2000), Constitutive law for permeability evolution of sandstone during depletion, paper presented at the International Symposium on Formation Damage Control, Soc. of Pet. Eng., Lafayette, La.
- Charalampidou, E.-M., S. A. Hall, S. Stanchits, H. Lewis, and G. Viggiani (2011), Characterization of shear and compaction bands in a porous sandstone deformed under triaxial compression, *Tectonophysics*, 503, 8–17, doi:10.1016/j.tecto.2010.09.032.
- Curran, J. H., and M. M. Carroll (1979), Shear stress enhancement of void compaction, *J. Geophys. Res.*, 84, 1105–1112, doi:10.1029/JB084iB03p01105.
- Dautriat, J., N. Gland, S. Youssef, E. Rosenberg, S. Bekri, and O. Vizika (2009), Stress-dependent directional permeabilities of two analog reservoir rocks: A prospective study on contribution of i-tomography and pore network models, *SPE Reservoir Eval. Eng.*, 12(2), 297–310, doi:10.2118/110455-PA.
- David, C., T. Wong, W. Zhu, and J. Zhang (1994), Laboratory measurement of compaction-induced permeability change in porous rock: Implications for the generation and maintenance of pore pressure excess in the crust, *Pure Appl. Geophys.*, 143, 425–456, doi:10.1007/BF00874337.

- Department of Energy (2007), Basic research needs for geosciences: Facilitating 21st century energy systems, report, 188 pp., Off. of Basic Energy Sci., Bethesda, Md.
- Eichhubl, P., W. L. Taylor, D. D. Pollard, and A. Aydin (2004), Paleo-fluid flow and deformation in the Aztec sandstone at the Valley of Fire, Nevada: Evidence for the coupling of hydrogeological, diagenetic, and tectonic processes, *Geol. Soc. Am. Bull.*, 116(9), 1120–1136, doi:10.1130/B25446.1.
- Eichhubl, P., J. N. Hooker, and S. E. Laubach (2010), Pure and shear-enhanced compaction bands in Aztec Sandstone, *J. Struct. Geol.*, 32, 1873–1886, doi:10.1016/j.jsg.2010.02.004.
- Flinn, D. (1962), On folding during 3D progressive deformation, *Q. J. Geol. Soc.*, 118, 385–428, doi:10.1144/gsjgs.118.1.0385.
- Fortin, J., A. Schubnel, and Y. Guéguen (2005), Elastic wave velocities and permeability evolution during compaction of Bleurwiller sandstone, *Int. J. Rock Mech. Min. Sci.*, 42(7–8), 873–889, doi:10.1016/j.ijrmms.2005.05.002.
- Fortin, J., S. Stanchits, G. Dresen, and Y. Guéguen (2006), Acoustic emission and velocities associated with the formation of compaction bands in sandstone, *J. Geophys. Res.*, 111, B10203, doi:10.1029/2005JB003854.
- Fossen, H., R. A. Schultz, and A. Torabi (2011), Conditions and implications for compaction band formation in the Navajo Sandstone, Utah, *J. Struct. Geol.*, 33, 1477–1490, doi:10.1016/j.jsg.2011.08.001.
- Freeze, R. A., and J. A. Cherry (1979), *Groundwater*, Prentice-Hall, Old Tappan, N. J.
- Heap, M. J., P. Baud, P. G. Meredith, A. F. Bell, and I. G. Main (2009), Time-dependent brittle creep in Darley Dale sandstone, *J. Geophys. Res.*, 114, B07203, doi:10.1029/2008JB006212.
- Heffer, K. (2002), Geomechanical influences in water injection projects: An overview, *Oil Gas Sci. Technol.*, 57, 415–422, doi:10.2516/ogst.2002027.
- Heiland, J., and S. Raab (2001), Experimental investigation of the influence of differential stress on permeability of a lower permian (Rotliegend) sandstone deformed in the brittle deformation field, *Phys. Chem. Earth, Part A*, 26, 33–38, doi:10.1016/S1464-1895(01)00019-9.
- Hill, R. E. (1989), Analysis of deformation bands in the Valley of Fire State Park, Nevada, MSc thesis, Univ. of Nevada, Las Vegas.
- Holcomb, D. J., J. W. Rudnicki, K. A. Issen, and K. Sternlof (2007), Compaction localization in the earth and laboratory, *Acta Geotech.*, 2, 1–15, doi:10.1007/s11440-007-0027-y.
- Hull, D. (1981), *An Introduction to Composite Materials*, Cambridge Univ. Press, Cambridge, U. K.
- Katsman, R., E. Aharonov, and H. Scher (2005), Numerical simulation of compaction bands in high-porosity sedimentary rock, *Mech. Mater.*, 37, 143–162, doi:10.1016/j.mechmat.2004.01.004.
- Keaney, G. M. J., P. G. Meredith, and S. A. F. Murell (1998), Laboratory study of permeability in a “tight” sandstone under non-hydrostatic stress conditions, paper presented at SPE/ISRM Eurock '98, Soc. of Pet. Eng., Trondheim, Norway.
- Keehm, Y., K. Sternlof, and T. Mukerji (2006), Computational estimation of compaction band permeability in sandstone, *Geosci. J.*, 10(4), 499–505, doi:10.1007/BF02910443.
- Klein, E., P. Baud, T. Reuschlé, and T. Wong (2001), Mechanical behaviour and failure mode of Bentheim sandstone under triaxial compression, *Phys. Chem. Earth*, 26, 21–25.
- Louis, L., C. David, and P. Robion (2003), Comparison of the behaviour of undeformed sandstones under dry and wet conditions, *Tectonophysics*, 370, 193–212, doi:10.1016/S0040-1951(03)00186-0.
- Louis, L., T. Wong, P. Baud, and S. Tembe (2006), Imaging strain localization by X-ray computed tomography: Discrete compaction bands in Diemelstadt sandstone, *J. Struct. Geol.*, 28, 762–775, doi:10.1016/j.jsg.2006.02.006.
- Louis, L., T. Wong, and P. Baud (2007), Imaging strain localization by X-ray computed microtomography and digital image correlation: Deformation bands in Rothbach sandstone, *J. Struct. Geol.*, 29, 129–140, doi:10.1016/j.jsg.2006.07.015.
- Louis, L., P. Baud, and T. Wong (2009), Microstructural inhomogeneity and mechanical anisotropy associated with bedding in sandstone, *Pure Appl. Geophys.*, 166, 1063–1087, doi:10.1007/s00024-009-0486-1.
- Main, I. G., K. Mair, O. Kwon, S. Elphick, and B. Ngwenya (2001), Recent experimental constraints on the mechanical and hydraulic properties of deformation bands in porous sandstones: A review, in *The Nature and Significance of Fault Zone Weakening*, edited by R. E. Holworth et al., *Geol. Soc. Spec. Publ.*, 186, 43–63.
- Menéndez, B., W. Zhu, and T. Wong (1996), Micromechanics of brittle faulting and cataclastic flow in Berea sandstone, *J. Struct. Geol.*, 18, 1–16, doi:10.1016/0191-8141(95)00076-P.
- Millien, A. (1993), Comportement anisotrope du grès des Vosges: Élastoplasticité, localisation de la rupture (in French), PhD thesis, Univ. Joseph Fourier, Grenoble, France.
- Mitchell, T. M., and D. R. Faulkner (2008), Experimental measurements of permeability evolution during triaxial compression of initially intact crystalline rocks and implications for fluid flow in fault zones, *J. Geophys. Res.*, 113, B11412, doi:10.1029/2008JB005588.
- Mollem, P. N., and M. A. Antonellini (1996), Compaction bands: A structural analog for anti-mode I cracks in aeolian sandstone, *Tectonophysics*, 267, 209–228, doi:10.1016/S0040-1951(96)00098-4.
- Olsson, W. A., and D. J. Holcomb (2000), Compaction localization in porous rock, *Geophys. Res. Lett.*, 27, 3537–3540, doi:10.1029/2000GL011723.
- Pons, A., C. David, J. Fortin, S. Stanchits, B. Menéndez, and J. M. Mengus (2011), X-ray imaging of water motion during capillary imbibitions: A study on how compaction bands impact fluid flow in Bentheim sandstone, *J. Geophys. Res.*, 116, B03205, doi:10.1029/2010JB007973.
- Rawlings, G., P. Baud, and T. Wong (2002), Dilatancy and anisotropy during brittle deformation of gneiss, *J. Geophys. Res.*, 107(B10), 2234, doi:10.1029/2001JB000472.
- Rudnicki, J. W. (2002), Conditions for compaction and shear bands in a transversely isotropic material, *Int. J. Solids Struct.*, 39, 3741–3756, doi:10.1016/S0020-7683(02)00173-7.
- Rudnicki, J. W. (2007), Models for compaction band propagation, in *Rock Physics and Geomechanics in the Study of Reservoirs and Repositories*, edited by C. David and M. LeRavalec, *Geol. Soc. Spec. Publ.*, 284, 107–126.
- Rudnicki, J. W., and J. R. Rice (1975), Conditions for the localization of deformation in pressure sensitive dilatant materials, *J. Mech. Phys. Solids*, 23, 371–394, doi:10.1016/0022-5096(75)90001-0.
- Schultz, R. A. (2009), Scaling and paleodepth of compaction bands, Nevada and Utah, *J. Geophys. Res.*, 114, B03407, doi:10.1029/2008JB005876.
- Sternlof, K. R., J. W. Rudnicki, and D. D. Pollard (2005), Anticrack inclusion model for compaction bands in sandstone, *J. Geophys. Res.*, 110, B11403, doi:10.1029/2005JB003764.
- Sternlof, K. R., M. Karimi-Fard, D. D. Pollard, and L. J. Durlofsky (2006), Flow and transport effects of compaction bands in sandstone at scales relevant to aquifer and reservoir management, *Water Resour. Res.*, 42, W07425, doi:10.1029/2005WR004664.
- Sun, W., J. E. Andrade, J. W. Rudnicki, and P. Eichhubl (2011), Connecting microstructural attributes and permeability from 3D tomographic images of in situ shear-enhanced compaction bands using multiscale computations, *Geophys. Res. Lett.*, 38, L10302, doi:10.1029/2011GL047683.
- Tembe, S., P. Baud, and T. Wong (2008), Stress conditions for the propagation of discrete compaction bands in porous sandstone, *J. Geophys. Res.*, 113, B09409, doi:10.1029/2007JB005439.
- Torabi, A., H. Fossen, and B. Alaei (2008), Application of spatial correlation functions in permeability estimation of deformation band in porous rocks, *J. Geophys. Res.*, 113, B08208, doi:10.1029/2007JB005455.
- Townend, E. (2007), An experimental study of compaction band evolution in an anisotropic sandstone, PhD thesis, 247 pp., Univ. of London, London.
- Townend, E., B. D. Thompson, P. M. Benson, P. G. Meredith, P. Baud, and R. P. Young (2008), Imaging compaction band propagation in Diemelstadt sandstone using acoustic emission locations, *Geophys. Res. Lett.*, 35, L15301, doi:10.1029/2008GL034723.
- Vajdova, V., P. Baud, and T. Wong (2004), Permeability evolution during localized deformation in Bentheim sandstone, *J. Geophys. Res.*, 109, B10406, doi:10.1029/2003JB002942.
- Walters, M. (1984), A study of the fracture toughness of slate and the determination of the Mohr envelope in the tensile field, MSc thesis, 101 pp., Univ. of London, London.
- Wang, B., Y. Chen, and T. Wong (2008), A discrete element model for the development of compaction localization in granular rock, *J. Geophys. Res.*, 113, B03202, doi:10.1029/2006JB004501.
- Wong, T., and W. Zhu (1999), Brittle faulting and permeability evolution: Hydromechanical measurement, microstructural observation, and network modeling, in *Faults and Subsurface Fluid Flow in the Shallow Crust*, *Geophys. Monogr. Ser.*, vol. 113, edited by W. Haneberg et al., pp. 83–99, AGU, Washington, D. C., doi:10.1029/GM113p0083.
- Wong, T., C. David, and W. Zhu (1997), The transition from brittle faulting to cataclastic flow in porous sandstones: Mechanical deformation, *J. Geophys. Res.*, 102, 3009–3025, doi:10.1029/96JB03281.
- Wong, T., P. Baud, and E. Klein (2001), Localized failure modes in a compactant porous rock, *Geophys. Res. Lett.*, 28, 2521–2524, doi:10.1029/2001GL012960.

- Wu, X. Y., P. Baud, and T. Wong (2000), Micromechanics of compressive failure and spatial evolution of anisotropic damage in Darley Dale sandstone, *Int. J. Rock Mech. Min. Sci.*, *37*, 143–160, doi:10.1016/S1365-1609(99)00093-3.
- Zhang, J., T. Wong, and D. M. Davis (1990), Micromechanics of pressure-induced grain crushing in porous rocks, *J. Geophys. Res.*, *95*, 341–352, doi:10.1029/JB095iB01p00341.
- Zhu, W., and T. Wong (1997), The transition from brittle faulting to cataclastic flow: Permeability evolution, *J. Geophys. Res.*, *102*, 3027–3041, doi:10.1029/96JB03282.
- Zhu, W., L. G. J. Montesi, and T. Wong (1997), Shear-enhanced compaction and permeability reduction: Triaxial extension tests on porous sandstone, *Mech. Mater.*, *25*, 199–214, doi:10.1016/S0167-6636(97)00011-2.